Structural iron in smectites with different charge locations

N. Finck[1] · **M. L. Schlegel**[2] · **K. Dardenne**[1] · **C. Adam**[1] · **S. Kraft**[1] · **A. Bauer**[1] · **J.-L. Robert**[3]

Abstract

The versatile structure of smectites can exhibit large variations in chemical compositions and cationic substitutions in different crystallographic sites, resulting in various locations of layer charge. Natural smectites can contain various amounts of structural iron, the chemical form of which can influence the reactivity of these minerals. The variety of Fe crystal chemistry in smectite was explored for eight natural smectites of distinct chemical compositions and charge locations, together with two synthetic ferric saponites used as reference compounds for tetrahedral Fe(III). All samples were identified as dioctahedral or trioctahedral smectite by X-ray diffraction and Fourier-transform infrared spectroscopy. The extent of $^{[4]}$Al for $^{[4]}$Si substitution was determined by ^{27}Al and ^{29}Si magic angle spinning nuclear magnetic resonance spectroscopy. The Fe local chemical environment was probed by polarized X-ray absorption spectroscopy. Only Fe(III) could be detected in all samples, with no evidence of cluster formation. The O shell at 1.86 Å in synthetic saponites suggests Fe insertion in tetrahedral sites, and the absence of detected octahedral Fe implies quantitative substitution of $^{[4]}Fe^{3+}$ for $^{[4]}Si^{4+}$. In natural smectites, Fe(III) is bound to six O atoms at ~2.00 Å, suggesting insertion in octahedral sites. This inference is also supported by the detection of in-plane Mg/Al/Fe atoms at ~3.05 Å and out-of-plane Si/Al atoms at ~3.25 Å. In one Fe-rich nontronite, the detection of an O subshell at ~1.88 Å suggests a concomitant insertion of Fe(III) in tetrahedral sites. Low numbers of octahedral neighbors were detected in natural saponite and hectorite, presumably because of the presence of vacancies and/or Li(I) in adjacent octahedral sites balancing the local charge excess originating from the substitution of Fe(III) for Mg(II). The substitution of $^{[4]}Fe^{3+}$ for $^{[4]}Si^{4+}$ can be readily obtained under defined conditions in the laboratory, but seems more rare in natural samples, or present in amounts below the detection limit of spectroscopic methods used in this study.

Keywords Smectites · Iron · Polarized XAS · FTIR · ^{27}Al and ^{29}Si MAS-NMR

Introduction

Smectites are part of the larger family of phyllosilicates (Bailey 1980). Smectites are made of one octahedral sheet bound between two tetrahedral sheets (Fig. 1) forming an assemblage known as *2:1 layer*. Only two-thirds of octahedral cationic sites are filled in dioctahedral phyllosilicates, whereas all octahedral sites are filled in trioctahedral ones (Bailey 1980). In the simplest form of 2:1 layers, the tetrahedral sheet contains only Si, the octahedral sheet either only Al^{3+} [pyrophyllite, $Al_2Si_4O_{10}(OH)_2$] or only Mg^{2+} [talc, $Mg_3Si_4O_{10}(OH)_2$] and the 2:1 layer has no permanent layer charge. Substitution of trivalent cations (e.g., Al^{3+} or Fe^{3+}) for Si^{4+} in the tetrahedral sheet, divalent cations (e.g., Mg^{2+}) for Al^{3+}, and vacancies or Li^+ for Mg^{2+} in the octahedral sheet results in a charge deficit in the 2:1 layer that is balanced by cations in the interlayer sheet. Smectites are 2:1 layers having a charge deficiency of < -0.6 per half-unit cell (Meunier 2005) and differ from other phyllosilicates in being hydrous, that is having water associated with surfaces and interlayer exchange cations. Smectites can exhibit large variations in chemical composition and in structural sites filling patterns as a consequence of their versatile structure, resulting in different locations of layer charge. In turn, the chemical reactivity of smectites is determined by the nature, the

N. Finck
nicolas.finck@kit.edu

[1] Institute for Nuclear Waste Disposal (INE), Karlsruhe Institute of Technology (KIT), P.O. Box 3640, 76021 Karlsruhe, Germany

[2] DEN-Service d'Etudes Analytiques et de Réactivité des Surfaces (SEARS), CEA, Université Paris-Saclay, 91191 Gif-sur-Yvette, France

[3] IMPMC, UMR 7590, CNRS-Université Pierre et Marie Curie, 4 place Jussieu, 75252 Paris Cedex 05, France

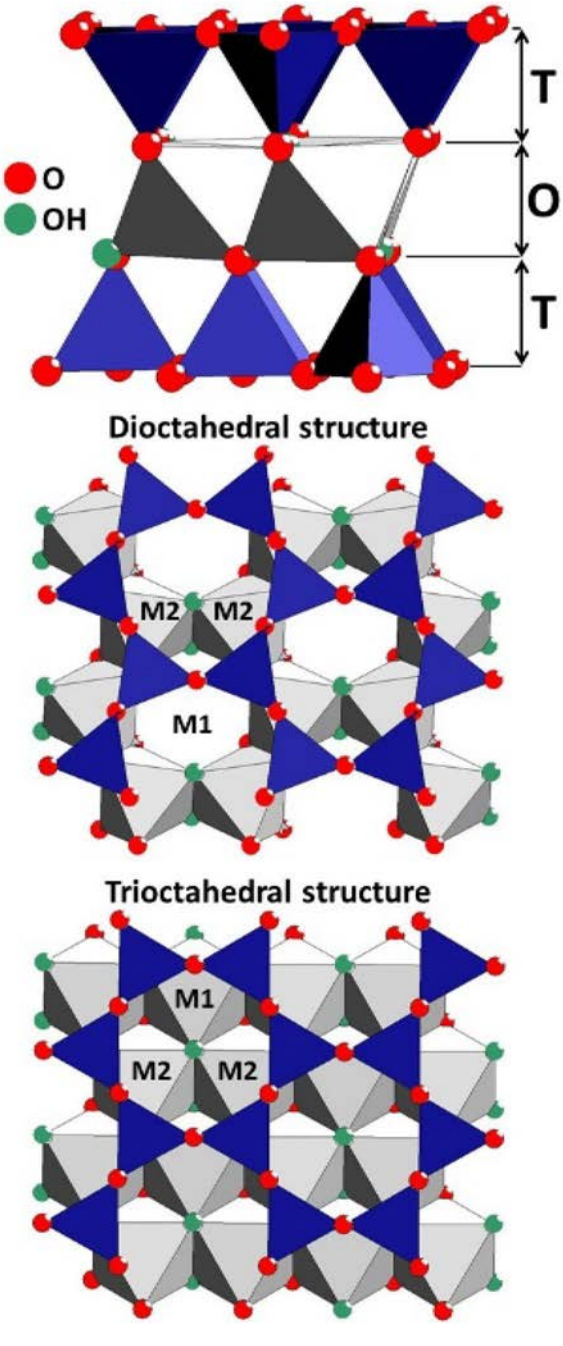

Fig. 1 Top: structure of smectites. T: tetrahedral sheet, O: octahedral sheet. Middle: projection down c^* of dioctahedral structure. Bottom: projection down c^* of trioctahedral structure. Blue triangles are $(Si,Al,Fe)O_4$ tetrahedra (one tetrahedral sheet is not shown). M1 denotes *trans* sites, M2 *cis* sites

distribution, and the extent of chemical substitution (Méring and Glaeser 1953).

Iron is the most abundant transition metal on Earth and a major component of many soil-forming parent minerals (Munoz et al. 2013; Prietzel et al. 2007). Consequently, most smectites formed in nature contain Fe from trace levels to large amounts. Depending on the redox conditions of geological settings, smectites may contain either Fe(II), Fe(III) or both at the same time. Ferrous iron fits well within octahedral sites ($^{[6]}$Fe(II) = 0.78 Å), but because of its large size compared to Si ($^{[4]}$Fe(II) = 0.63 Å, $^{[4]}$Si(IV) = 0.26 Å) (Shannon 1976), it may only hardly substitute for tetrahedral Si within smectites. In contrast, the smaller ferric iron can occupy tetrahedral ($^{[4]}$Fe(III) = 0.49 Å) as well as octahedral sites ($^{[6]}$Fe(III) = 0.65 Å).

Structural Fe within smectites can have a significant impact on redox properties in environments where these minerals are present. Structural Fe(II) in clay minerals is able to reduce heavy metals, radionuclides, and organic contaminants, thereby altering their mobility and (bio)availability (Bishop et al. 2011; Hofstetter et al. 2006; Jaisi et al. 2009; Joe-Wong et al. 2017). In contrast, structural Fe(III) can act as a terminal electron acceptor for Fe-reducing bacteria, and the electron transfer provides a mechanism of structural Fe(II) (re)generation (Dong et al. 2009; Ernstsen et al. 1998). Likewise, changes in the oxidation state of Fe in clay minerals play an important role in determining the chemical and physical properties of soils and sediments in which these minerals are present. As a consequence of Fe(III) reduction in smectites, the specific surface area decreases (Lear and Stucki 1989), the cation exchange capacity increases (Favre et al. 2002), swelling in water decreases (Stucki et al. 1984b), and the reactivity with pollutants (Khaled and Stucki 1991) and the potential for mineral dissolution and transformation increase (Stucki et al. 1984a). For performance assessment of disposal sites for pollutants, such as, for example, radioactive waste, this kind of information is of crucial importance. Consequently, the accuracy and reliability of performance assessment depend on the precise characterization of materials used to construct barriers (e.g., engineered barriers made of bentonite), with greater attention devoted to structural elements such as iron.

The extent and reversibility of Fe reduction/oxidation depend on the Fe crystallochemical environment (Drits and Manceau 2000). For example, in reduced Wyoming montmorillonite SWy-2, only one reactive Fe(II) species, octahedral $AlFe^{2+}$–OH, can be identified; a full reduction/oxidation cycle restores the original structure (Neumann et al. 2011). In contrast, reduction of the Fe-rich SWa-1 and Ölberg montmorillonites results in the formation of multiple Fe(II) entities and is accompanied by intense dehydroxylation and structural rearrangements (Stucki and Roth 1977) which are only partially reversible by re-oxidation (Gates et al. 1996; Fialips et al. 2002; Neumann et al. 2011). It has also been suggested that the overall cationic composition and the location of the layer charge affect the reactivity of structural Fe(II) species (Neumann et al. 2011). Reported redox profiles of dioctahedral smectites, representing the fraction of reduced Fe as a function of applied potential, seem to depend on the charge location in addition to the layer charge and to the Fe content (Gorski et al. 2013). For example, for increasing Fe content or for increasing layer charge, more negative potentials are needed to reduce structural Fe(III). These above-mentioned studies highlight the importance of Fe crystallochemistry on smectite reactivity. Detailed studies on the distribution of Fe in smectites have been reported (Gates et al. 2002; Manceau et al. 2000; Vantelon et al. 2003), including for reduced smectites (e.g., Manceau et al. 2000; Neumann et al. 2011); however, they were restricted to dioctahedral smectites only.

In this study, a series of eight natural smectites and two synthetic trioctahedral smectites having different structures, layer charges, and charge locations was used to explore the variety of Fe crystallochemistry by applying complementary analytical techniques. The goal was to determine the distribution of Fe within structural sites of smectites and to characterize the local chemical environment. All natural smectites underwent similar purification and fractionation procedures. Synthetic saponites containing $^{[4]}Fe^{3+}$ partially substituting for $^{[4]}Si^{4+}$ were used as reference compounds. All compounds were first discriminated as dioctahedral or trioctahedral smectites by X-ray diffraction (XRD) and Fourier-Transform Infrared (FTIR) spectroscopy, and the distribution of Al between the tetrahedral and the octahedral sheet was determined by ^{27}Al magic angle spinning nuclear magnetic resonance (MAS-NMR) spectroscopy. Finally, self-supporting films were prepared for all samples and the Fe environment was probed by Fe *K*-edge polarized X-ray Absorption Spectroscopy (XAS). This technique allows to single out the Extended X-ray Absorption Fine Structure (EXAFS) contributions of next nearest octahedral and tetrahedral cationic neighbors surrounding an octahedral cation, and which strongly overlap in powder XAS (Manceau 1990; Manceau et al. 1998, 2000; Schlegel et al. 1999).

Experimental

Materials

Eight smectites were purchased from the Source Clay Repository of the Source Clay Mineral Project. These are dioctahedral montmorillonites (SWy-2, SAz-1, STx-1) and nontronites (yellowish-green NAu-1, dark-brown NAu-2, greenish NG-1), and trioctahedral hectorite (SHCa-1) and saponite (SapCa-2). Raw materials were first converted to the Na form by repeatedly washing with 1 M NaCl. Except for nontronites, materials were subsequently treated shortly with HCl at pH 3–4 in 1 M NaCl (to remove accessory carbonate phases) and brought back to neutral conditions by washing with 1 M NaCl. No chemical treatment such as that using dithionite to remove admixed Fe phases (e.g., Moore and Reynolds 1997) was applied, as it would alter structural Fe speciation. Instead, the fraction < 0.1 µm was separated by successive sedimentation and centrifugation steps to remove most impurities. Chemical analyses of these samples are given in Table 1. In addition, two synthetic trioctahedral smectites were used in this study: a saponite containing tetrahedral ferric iron (Sapo-Fe) and a second saponite containing Fe(III) and Al(III) substituting for Si(IV) in the tetrahedral sheet (Sapo-FeAl). Synthetic saponites were prepared from gels of appropriate compositions. Gels were slowly dried at ~ 200 °C and then calcined at 600 °C. The resulting materials were crushed and placed in Morey-type pressure vessels. Samples were taken out after 4 weeks heating at 400 °C and 1000 bar water pressure. Details about synthesis can be found elsewhere (Michot et al. 2005). Synthetic smectites were used without purification and fractionation. Chemical compositions of natural samples were obtained by X-ray fluorescence spectroscopy analyses, except NG-1 for which energy-dispersive X-ray spectroscopy (SEM-EDX,

Table 1 Chemical composition of studied natural smectites as determined by XRF on ignited samples, except for NG-1

Sample	(%)													
	SiO_2	Al_2O_3	Fe_2O_3	MgO	Cr_2O_3	MnO	NiO	TiO_2	Na_2O	K_2O	CaO	P_2O_5	SO_3	Sum
SWy-2	65.35	23.82	4.81	2.81	0.001	0.01	0.000	0.111	3.05	0.03	0.05	0.02	0.00	100.06
SAz-1	67.68	20.04	1.84	6.56	0.003	0.02	0.001	0.260	4.10	0.02	0.06	0.01	0.00	100.60
STx-1	68.98	21.37	1.18	4.00	0.001	0.01	0.000	0.290	3.28	0.02	0.05	0.03	0.03	99.24
SHCa-1[a]	66.34	0.56	0.25	29.32	0.002	0.00	0.002	0.031	2.70	0.07	0.06	0.01	0.00	99.35
SapCa-2	58.91	5.23	1.39	31.48	0.002	0.02	0.000	0.020	2.97	0.02	0.09	0.01	0.05	100.19
NAu-1	51.29	9.07	34.81	0.19	0.020	0.00	0.005	0.020	3.68	0.01	0.04	0.01	0.03	99.18
NAu-2	56.73	3.25	37.37	0.16	0.004	0.00	0.010	0.030	2.66	0.01	0.04	0.02	0.00	100.28
NG-1	48.76	2.70	36.31	0.44	–	–	–	–	3.20	–	–	–	–	91.41

Chemical composition of sample NG-1 was determined by SEM-EDX, and accounting for water content (~ 8.4 wt% by thermal analysis)

[a] Sample SHCa-1 contains ~ 3 wt% fluorine (Thomas et al. 1977) and 0.53 wt% Li determined by sample acidic digestion and quantification by ICP-OES

FEI Quanta 650 FEG) analysis was applied. Structural formulae were determined by combining all results from this study.

Methods

For all samples, XRD patterns were recorded under ambient conditions on a D8 Advance (Bruker) diffractometer (Cu $K\alpha$ radiation) equipped with an energy-dispersive detector (Sol-X). Powder patterns were recorded from 2° to 70° 2θ, with a step size of 0.04° and a counting time of 45 s per step. The absolute precision of Bragg angles was estimated to 0.01° 2θ over the whole angular range. Values of $c^* = 4 \times d(004)$, $b = 6 \times d(060)$ and $a = b/\sqrt{3}$ (Brindley 1980) were determined from modeling of experimental patterns in the angular ranges 24°–33° 2θ for $d(004)$ and 57°–67° 2θ for $d(060)$.

The FTIR spectra were recorded for powdered samples under ambient conditions using an IFS 55 spectrometer (Bruker) equipped with an attenuated total reflectance (ATR) accessory and a solid-state DTGS detector. The spectral resolution is 4 cm^{-1}.

The MAS-NMR spectra were recorded at 300 K on a Bruker Advance III 400 wide-bore spectrometer operating at 400.18 MHz for ^{1}H, 104.27 MHz for ^{27}Al and 79.50 MHz for ^{29}Si, respectively. The spectrometer was equipped with a 4 mm Cross Polarization (CP) MAS probe. Disposable Kel-F inserts (approx. 30 µL volume) were filled with powdered samples and inserted into 4 mm ZrO_2 MAS rotors. For ^{27}Al direct observation methods were used. The MAS rotation frequency was 15 kHz and standard Bruker 1D pulse sequences with 90° pulse angle were used. Spectra were recorded with 16 k data points. Because samples contain paramagnetic Fe, the relaxation delay was 250 ms. 4096 scans were recorded for each spectrum. For ^{29}Si, CP was used whenever possible. The rotation frequency was 12.5 kHz, the $n = 1$ sideband conditions were calculated, and contact time and ^{1}H pulse power were optimized before acquisition. Optimal contact times were about 7 ms for most samples. The acquisition time was approximately 100 ms depending on the contact time, corresponding to approximately 1500 data points sampled in the Free Induction Decay (FID). Typically, 2 k scans were averaged for each spectrum. In the more paramagnetic samples, CP could not be achieved due to the increased relaxation; therefore, direct excitation spectra with high-power proton decoupling were used. The acquisition time was set to 100 ms, corresponding to 1588 data points in the FID, the SPINAL64 decoupling sequence was used for proton decoupling. Typically, 16–64 k scans were averaged per sample. Delay times between individual scans were 2.5 s in CP experiments and 5 s for direct acquisition. For processing, exponential window functions with a line-broadening factor of 5 Hz and zero-filling to 32 k data points were used, and relative intensities of components determined by integration. Because of the appreciable noise level (low Al content and/or high Fe content), estimated errors in chemical shifts and in relative signal intensities amount to at least 1–2 ppm and 5–10%, respectively.

Fe K-edge XAS data were recorded at the INE-beamline (Rothe et al. 2012) at the KIT Synchrotron Light Source (Karlsruhe, Germany) with a storage ring energy of 2.5 GeV, and at the BM30B beamline (Proux et al. 2006) at the European Synchrotron Radiation Facility (ESRF, Grenoble, France) with a storage ring energy of 6.0 GeV. At the INE beamline, the incident X-ray beam was monochromatized using a pair of Si(111) crystals, and spectra were recorded either in transmission or in fluorescence mode using a silicon drift detector (Vortex-60EX, SII Nano Technology). At the BM30B beamline, a pair of Si(220) crystals was used to monochromatize the incident X-ray beam, and spectra were recorded either in transmission or in fluorescence mode using a 30-element Ge detector (Canberra). At both stations, the energy was calibrated by assigning the first inflection point of the K-edge XANES recorded from an Fe foil to 7112 eV.

For polarized XAS measurements, smectites were prepared as self-supporting films by slow vacuum filtration of suspensions on mixed cellulose esters filters of 0.025 µm pore size (Millipore). This protocol readily provided highly textured samples with a- and b-axes randomly oriented in the film plane (Manceau et al. 1998). Two to three slices of the same film (only one slice for nontronites) were cut and stacked on a holder to prepare a sample for polarized XAS measurements. Self-supporting films were mounted on a goniometer and spectra were recorded at angles (α) between the electric field of the X-ray beam and the clay layer plane of 10°, 35°, 55°, and 80°, except for STx-1 for which the spectrum at 10° was calculated by extrapolation using experimental data at 35°, 55°, and 80° (Schlegel et al. 1999). The experimental uncertainty related to the selection of α during XAS measurements is estimated to $\pm 1°$.

XAS data were analyzed following standard procedures using Athena and Artemis interfaces to the Iffefit software (Ravel and Newville 2005). EXAFS spectra were extracted from the raw data and Fourier transforms (FT) were obtained from the $k^3 \times \chi(k)$ functions. Data were fit in R-space using phase and amplitude functions calculated with feff8.4 (Ankudinov et al. 1998), and the amplitude reduction factor was set to 0.88. Theoretical paths were generated using published structures of montmorillonite (Tsipursky and Drits 1984), hectorite (Breu et al. 2003) and nontronite (Manceau et al. 1998) with the absorber (Fe) located at octahedral position, and tetraferriphlogopite (Semenova et al. 1977) with Fe located at tetrahedral position. Since differences in backscattering amplitudes between Mg, Al, and Si are limited, XAS models were simplified. In montmorillonites, only Al and Si backscatterers were considered to fit octahedral and tetrahedral contributions, respectively; in hectorite and saponites, only Mg (octahedral) and Si (tetrahedral) atoms were considered; in nontronites, only tetrahedral Si atoms were used, as explained in greater detail below. In all samples, the presence of neighboring Fe atoms was assessed. Though hectorite contains –F substituting for –OH groups (Thomas et al. 1977), the Fe first coordination shell was considered to be made of only O atoms for fitting purposes (O and F only differ by Z ± 1). For octahedral Fe, additional O shells were considered beyond the closest octahedral and tetrahedral shells: these are O atoms from edge-sharing octahedra and next nearest O atoms from the tetrahedral sheet. Considering their location within the structure, they are expected to exhibit significant angular dependences. Since ab initio EXAFS modeling showed the limited importance of multiple-scattering paths at distances larger than ~ 3.70 Å in nontronite (Manceau et al. 1998), only single scattering paths were used in the fitting procedure of all samples, in agreement with earlier studies (e.g., Manceau et al. 1998, 2000; Finck et al. 2015). For a given film, data were fit simultaneously at all angles using a single value of shift in ionization energy (ΔE_0), and for a given atomic shell a common bond length and mean square displacement ("Debye–Waller" term) (Finck et al. 2009; Schlegel and Manceau 2013). For every sample the Fe/Al (montmorillonites), Fe/Mg (hectorite, natural saponite) and Fe/Si (synthetic saponites) ratios were kept equal at all angles.

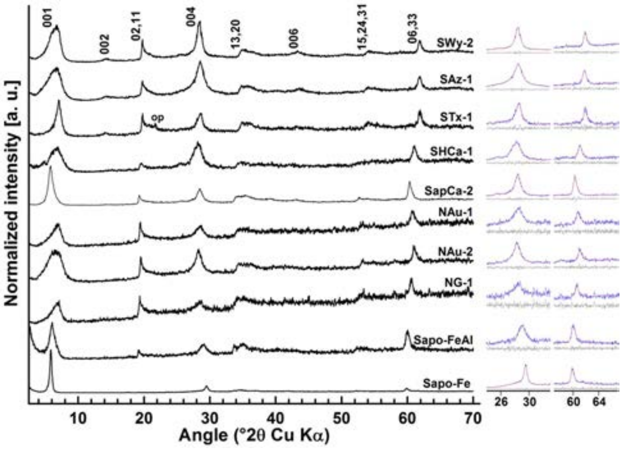

Fig. 2 Powder X-ray diffractogram of the studied smectites recorded under ambient conditions. Diffraction maxima are indexed. "op" indicates opal impurity in STx-1 sample. Experimental and modeled diffractograms in the angular ranges 24–33° 2θ ($d(004)$) and 57–67 °2θ ($d(060)$) are shown on the right side, results are presented in Table 2

Table 2 Unit cell parameters derived from XRD analysis of powdered samples (Fig. 2)

Sample	$c^* = 4 \times d(004)$ [Å]	$b = 6 \times d(060)$ [Å]	$a = b$
SWy-2	12.52	8.99	5.19
SAz-1	12.50	8.99	5.19
STx-1	12.48	8.98	5.19
SHCa-1	12.65	9.11	5.26
SapCa-2	12.54	9.20	5.31
NAu-1	12.50	9.14	5.28
NAu-2	12.64	9.11	5.26
NG-1	12.51	9.16	5.29
Sapo-Fe	12.10	9.27	5.35
Sapo-FeAl	12.29	9.23	5.33

Results

X-ray diffraction and infrared spectroscopy

Powder XRD patterns (Fig. 2) identified all samples as phyllosilicates. Patterns display only basal reflections (001, 002, 004, and 006) and two-dimensional *hk* bands (02,11; 13,20; 15,24,31; and 06,33) as a consequence of the turbostratic stacking of layers (Brindley 1980). Important differences can be observed in the position of the 06,33 bands which provide information on the structure in the *ab* plane (Brindley 1980; Moore and Reynolds 1997), namely, the distinction between dioctahedral and trioctahedral framework, because the *b* cell dimension is sensitive to the size of the cations and to the site occupancy in the octahedral sheet. All *b* cell dimensions are comparable to reported values (Brindley 1980; Manceau et al. 2000; Mering and Oberlin 1967). Montmorillonites have the smallest *b* dimension (8.98–8.99 Å, Table 2) which is due to only two-third of octahedral sites filling by Al^{3+}. The values of *b* (9.11–9.16 Å) are larger for nontronites because of octahedral sites filled by the large $^{[6]}Fe^{3+}$ ($r = 0.65$ Å) compared to $^{[6]}Al^{3+}$ ($r = 0.54$ Å) (Shannon 1976). Trioctahedral hectorite has octahedral sites mostly filled with Mg^{2+} ($r = 0.72$ Å), along with Li^+ ($r = 0.76$ Å), and has a *b* value ($b = 9.11$ Å) comparable to that of the nontronites. The largest *b* values ($b = 9.20$–9.27 Å) were obtained for saponites which contain $^{[4]}Al^{3+}$ ($r = 0.39$ Å) or $^{[4]}Fe^{3+}$ ($r = 0.49$ Å) substituting for $^{[4]}Si^{4+}$ ($r = 0.26$ Å) that increases the dimensions of the tetrahedral layer, and the *b* value increases with the Fe content. *c* values are typical of one hydration water layer in the interlayer (Meunier 2005). No accessory crystalline phase could be detected in any sample except trace amounts of opal (cristobalite-like phase) in STx-1.

The FTIR spectra (Fig. 3) of SWy-2, SAz-1 and STx-1 contain bands at 911 cm^{-1}, 879 cm^{-1}, 842 cm^{-1} and 795 cm^{-1} corresponding to Al_2^{3+}–OH, $Fe^{3+}Al^{3+}$–OH, $Al^{3+}Mg^{2+}$–OH and $Fe^{3+}Mg^{2+}$–OH bending, respectively. The differences in band intensities indicate variability in

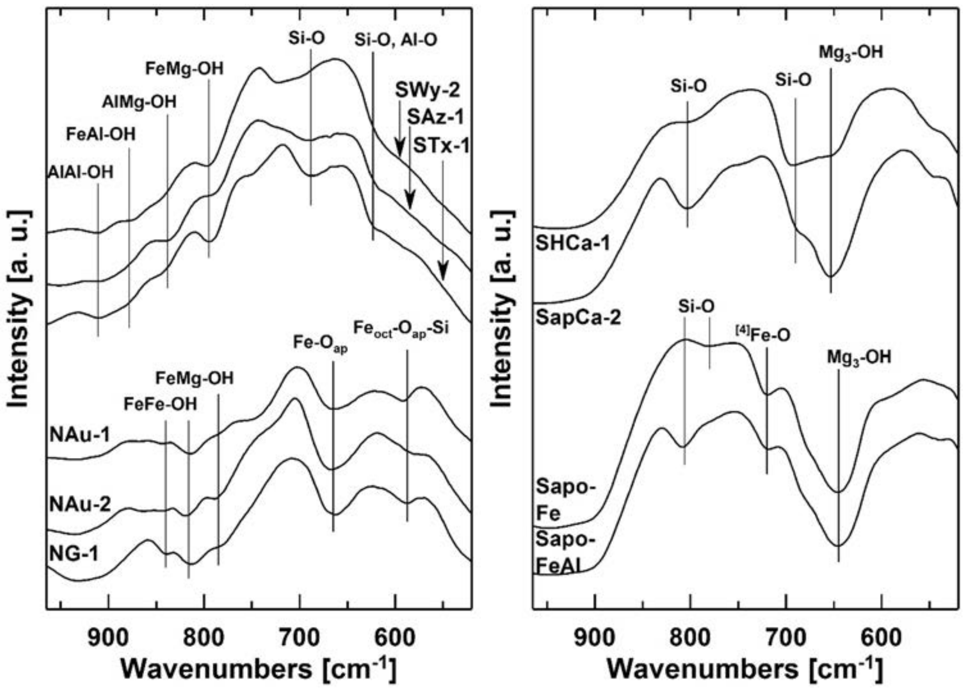

Fig. 3 Fourier-transform infrared (FTIR) spectra of the –OH-bending region of smectites investigated in this study

the nature of cationic pairs filling octahedral sites, in agreement with differences in chemical compositions (Gates 2008; Madejova and Komadel 2001). In the STx-1 spectrum, the band near 790 cm^{-1} is of slightly higher intensity than in the spectrum of SWy-2 and SAz-1. In agreement with results from XRD analysis, this band hints at the presence of cristobalite-like phase impurities (Madejova and Komadel 2001). The spectra contain additional bands near 690 cm^{-1} and 625 cm^{-1} that can be attributed to Si^{4+}–O and to coupled Si–O and Al–O out-of-plane deformation, respectively (Madejova and Komadel 2001).

Bands at 840 and 816 cm^{-1} in the spectra of nontronites are assigned to Fe$^{3+}{}_2$–OH bending (Baron et al. 2016; Gates 2008) and that at 863 cm^{-1} to Fe^{3+}Al^{3+}–OH bending (Fig. 3). The weak band at 787 cm^{-1} can be assigned to Fe^{3+}Mg^{2+}-OH bending and the band at 665 cm^{-1} to Fe–O$_{ap}$ out-of-plane deformation. The band near 585 cm^{-1} assigned to Fe$^{3+}{}_{oct}$–O$_{ap}$–Si$^{4+}{}_{tet}$ lattice deformation is only visible for nontronites, not for the other smectites. The presence of trace amounts of admixed kaolinite in STx-1 and NAu-1 is suggested from the hydroxyl-stretching region of the spectra (data not shown), but its presence in these samples could not be detected by XRD. Note that the higher Fe content of nontronites compared to montmorillonites caused a shift in position of the Fe^{3+}Al^{3+}–OH and Fe^{3+}Mg^{2+}–OH-bending bands to slightly lower wavenumbers, in agreement with earlier findings (Gates 2005).

The spectra of SHCa-1, SapCa-2, and both synthetic saponites (Fig. 3) display a band near 650 cm^{-1} attributed to Mg$_3{}^{2+}$–OH deformation, which is diagnostic of a trioctahedral framework (Madejova and Komadel 2001). The spectra of SapCa-2 and Sapo-FeAl also contain a band near 803 cm^{-1}, which is less intense in the spectrum of the hectorite, indicating the presence of silica (Madejova and Komadel 2001). The spectrum of the natural samples also contains a Si^{4+}–O deformation band at 690 cm^{-1}. Interestingly, a band is present at 720 cm^{-1} in the spectra of the synthetic saponites but is absent in all other spectra, and can tentatively be assigned to $^{[4]}$Fe^{3+}–O vibration, compared to values reported by Baron et al. (707 cm^{-1}; Baron et al. 2016) and Neumann et al. (714 cm^{-1}; Neumann et al. 2011). The slightly higher intensity of this band in Sapo-Fe compared to Sapo-FeAl can tentatively be attributed to the higher $^{[4]}$Fe^{3+} content (Baron et al. 2016).

In conclusion, XRD and FTIR data indicate that samples are free from Fe-containing impurities, only low amounts of SiO$_2$ or trace amounts of kaolinite could be detected in some samples.

MAS-NMR spectroscopy

Octahedral and tetrahedral Al^{3+} can be distinguished by ^{27}Al MAS-NMR spectroscopy and are characterized by chemical shifts of ~5 ppm and ~70 ppm, respectively (Sanz and Serratosa 1984a, b). Spectra were recorded for all samples except for NAu-2, NG-1, and Sapo-Fe because of the absence of, or low Al content, or because of high amounts of paramagnetic Fe^{3+}. Low Al or high Fe contents also resulted in very noisy spectra for Sapo-FeAl and NAu-1 (Fig. 4). Spectra contain either one or two components and their

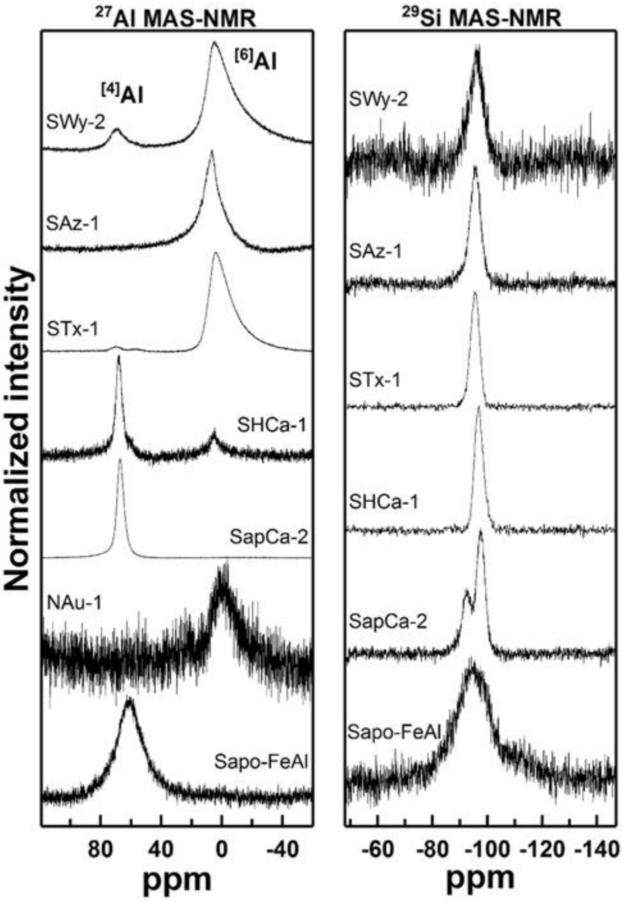

Fig. 4 Experimental ^{27}Al and ^{29}Si MAS-NMR spectra of smectites, values of chemical shifts and integrals are presented in Table 3. For samples NAu-2 and NG-1 the Al content was too low and the Fe content too high for ^{27}Al MAS-NMR spectroscopy, sample Sapo-Fe does not contain Al. The Fe content of the nontronites and SapoFe was too high for ^{29}Si MAS-NMR spectroscopy

integrals provide information on the partition of Al between octahedral and tetrahedral sites (Table 3). No $^{[4]}$Al could be detected in SAz-1, whereas SWy-2 and STx-1 contain low amounts of $^{[4]}$Al. In contrast, spectra show the absence of $^{[6]}$Al in SapCa-2 and Sapo-FeAl, and the presence of moderate amounts of $^{[6]}$Al in SHCa-1.

The spectrum of NAu-1 (Fig. 4) indicates the presence of only $^{[6]}$Al although Al is expected to be distributed between tetrahedral and octahedral sites in nontronite (Keeling et al. 2000). Actually, NAu-1 has a very high Fe content (~ 24 wt% Fe) in the octahedral sheet and the quick relaxation of unpaired electrons of paramagnetic Fe^{3+} leads to strong fluctuations in the magnetic field experienced by the nuclei under observation (e.g., Labouriau et al. 1996; Sanz and Serratosa 1984b). Through dipolar coupling of the strong electrons spins to the quickly relaxing electronic spins, an effective pathway for nucleus T_1 (spin–lattice or longitudinal relaxation) and T_2 (spin–spin or transversal relaxation) relaxation is formed and nuclear relaxation is enhanced. This leads to broadening of the NMR signals, and when Fe^{3+} is present in significant amounts (as is the case for our samples), the signal is effectively bleached in the vicinity of paramagnetic centers. Although the signal is lost only within a radius of 6 Å around Fe^{3+}, there is hardly any structural Al at larger distance within the structure of nontronites because of nearly quantitative octahedral sites filling by Fe^{3+}. Therefore, the only plausible explanation is the detection of $^{[6]}$Al from trace amounts of admixed kaolinite impurities detected by FTIR spectroscopy. Similarly, the wider $^{[4]}$Al signal in Sapo-FeAl compared to SapCa-2 or SHCa-1 can be attributed to the higher Fe content.

In smectites, Si atoms are only located in tetrahedral sites and each SiO_4 tetrahedron shares corners with three neighboring tetrahedra, while the fourth corner (apical oxygen atom) is shared with three octahedra. In smectites $^{[4]}$Si can also be substituted by $^{[4]}$Al and sometimes by $^{[4]}Fe^{3+}$, so that Si atoms are connected to two Si and one tetrahedral Al/

Table 3 ^{27}Al and ^{29}Si MAS-NMR parameters [chemical shifts (ppm) and proportions (%)] deduced from experimental spectra presented in Fig. 4

Sample	$^{[4]}$Al		$^{[6]}$Al		Si(3Si)		Si(2SiAl)	
	ppm	%	ppm	%	ppm	%	ppm	%
SWy-2	70	5	5	95	− 96	100	–	–
SAz-1	–	–	7	100	− 95	100	–	–
STx-1	70	1.5	4	98	− 95	100	–	–
	57[a]	0.5	–	–				
SHCa-1	68	77	5	23	− 97	100	–	–
SapCa-2	67	100	–	–	− 98	67	-93	33
NAu-1	–	–	2	100	–	–	–	–
Sapo-FeAl	61	100	–	–	− 95[b]	100	–	–

[a] Denotes impurities

[b] Only one broad band was observed for Sapo-FeAl, which may correspond to a convolution of Si(3Si) and Si(2SiAl) contributions which could not be resolved

Fe, and such modifications in local chemical environment can be detected by ^{29}Si MAS-NMR (e.g., Sanz and Serratosa 1984b). The NMR spectrum of all samples contains a band located around − 95 to − 98 ppm (Fig. 4; Table 3) which corresponds to Si connected to three neighboring Si atoms (Si(3Si)) (Cadars et al. 2012; Komarneni et al. 1986; Labouriau et al. 1996). Differences in chemical shifts between the samples are a consequence of both structural distortions in the tetrahedral sheet and compositional variation in the octahedral sheet (Labouriau et al. 1996). The spectrum of SapCa-2 contains in addition a second band at − 93 ppm arising from Si connected to two Si and one tetrahedral Al [Si(2SiAl)], which agrees with Al for Si substitution in saponite. In SHCa-1, Al is mainly located in the tetrahedral sheet; however, the Al content is too low to give rise to a second band in the ^{29}Si MAS-NMR spectrum [i.e., Si(2SiAl) band]. Compared to the spectra of natural smectites, the band in the spectrum of Sapo-FeAl is considerably wider. The width of this band can hardly be explained by a single contribution and, according to the chemical composition, may best be explained by the convolution of signals from Si located in different local environments, such as, e.g., Si connected to three Si and Si connected to two Si and one tetrahedral Al/Fe. Note that in samples containing significant amounts of Fe, lines are considerably broadened by paramagnetic interactions (Sanz and Serratosa 1984b). No additional band can be seen in the ^{29}Si MAS-NMR spectrum of Sapo-FeAl implying that if silica is present (as a byproduct of the clay synthesis), as suggested by FTIR; then, its amount must be low. Similarly, data also exclude the presence of significant amounts of admixed silica phase in the natural smectites (e.g., the spectrum of STx-1 does not contain any band around ~ − 107 ppm; Lippmaa et al. 1980).

According to MAS-NMR results, montmorillonites have low $^{[4]}$Al^{3+} for $^{[4]}$Si^{4+} substitution, whereas SapCa-2 has significant $^{[4]}$Al^{3+} for $^{[4]}$Si^{4+} substitution and most of Al contained in SHCa-1 is located in the tetrahedral sheet. These findings are in agreement with earlier studies on montmorillonites, saponite and hectorite (Cadars et al. 2012; Komarneni et al. 1986; Morris et al. 1990; Woessner 1989).

X-ray absorption spectroscopy

Polarized XAS is a powerful method to single out in-plane and out-of-plane EXAFS contributions of elements in sheet silicates. However, its application critically depends on the texture of the sample, i.e., on the orientation distribution of the c^* axis of platelets (Manceau and Schlegel 2001).

XANES spectroscopy

The pre-edges of montmorillonites, SHCa-1, SapCa-2, and nontronites are of low intensity, whereas the pre-edges of Sapo-Fe and Sapo-FeAl are of significantly higher intensity (Fig. 5). Compared to the reported data of $^{[6]}$Fe and $^{[4]}$Fe reference compounds (e.g., Westre et al. 1997; Wilke et al. 2001), these features hint at prevalence of octahedral coordination in the natural samples and at prevalence of tetrahedral coordination in the synthetic compounds.

The energy position of experimental Fe *K*-edge powder XANES (i.e., at $\alpha = 35°$) of all smectites indicates the presence of prevailing Fe^{3+} (Fig. 5; Waychunas et al. 1983). The XANES of the montmorillonites, SHCa-1 and SapCa-2 look very similar to one another, from the shape of the edge or white line (WL) to the post-edge region, hinting at very similar environments in terms of type and number of coordinating atoms and interatomic distances. The XANES of the nontronites differ slightly in shape of the first resonance at ~ 7200 eV, hinting at distinct chemical environments in terms of type of neighboring atoms. Both synthetic saponites have similar XANES signatures, which clearly differ from those of all other smectites. Their WL height is lower and the shoulder at ~ 7148 eV is of much higher intensity compared to the other smectites, reflecting photoelectric multiple-scattering effects at medium-range distance around the absorber (Munoz et al. 2013). The observed differences in XANES between both synthetic saponites and the other smectites can best be attributed to differences in coordination geometries such as, e.g., T_d in the former and O_h in the latter. This would agree with the presence of the band at 720 cm^{-1} attributed to $^{[4]}$Fe–O in the FTIR spectra of the synthetic smectites (Fig. 3). In the post-edge region of Sapo-Fe and Sapo-FeAl, the first resonance located at ~ 7200 eV also significantly differs from that of the other smectites, providing further evidence for differences in the Fe first coordination sphere.

The XANES of all smectites exhibit significant angular dependences (Figs. 7, 8, 9, 10). The amplitude of the WL decreases with increasing α values, hinting at an in-plane orientation, and the post-edge regions contain well-defined isosbestic points, which attest to the high degree of particles orientation within the films. Variations in amplitude and sometimes the position of the resonance centered at ~ 7200 eV evidence the presence of atomic shells with distinct orientations.

EXAFS spectroscopy

The powder EXAFS spectra of the montmorillonites look very similar to one another in terms of position and amplitude of the oscillation maxima (Fig. 5). The spectrum of SHCa-1 slightly differs from that of the montmorillonites, mainly in the position of the oscillation maximum at $k \sim 5.4$ Å^{-1} compared to $k \sim 5.0$ Å^{-1} in the montmorillonites. The spectrum of SapCa-2 differs from that of SHCa-1 by the feature at $k \sim 7.5$ Å^{-1} and the lower amplitude of oscillations at $k > 7$ Å^{-1}. The spectra of the nontronites have

Fig. 5 Experimental Fe *K*-edge powder ($\alpha = 35°$) XANES (left panel) and experimental (solid black line) and modeled (red symbols) powder EXAFS spectra (right panel) of all smectites. The corresponding Fourier transforms are shown in Fig. 6. Fit results are presented in Tables 4, 5, 6, and 7

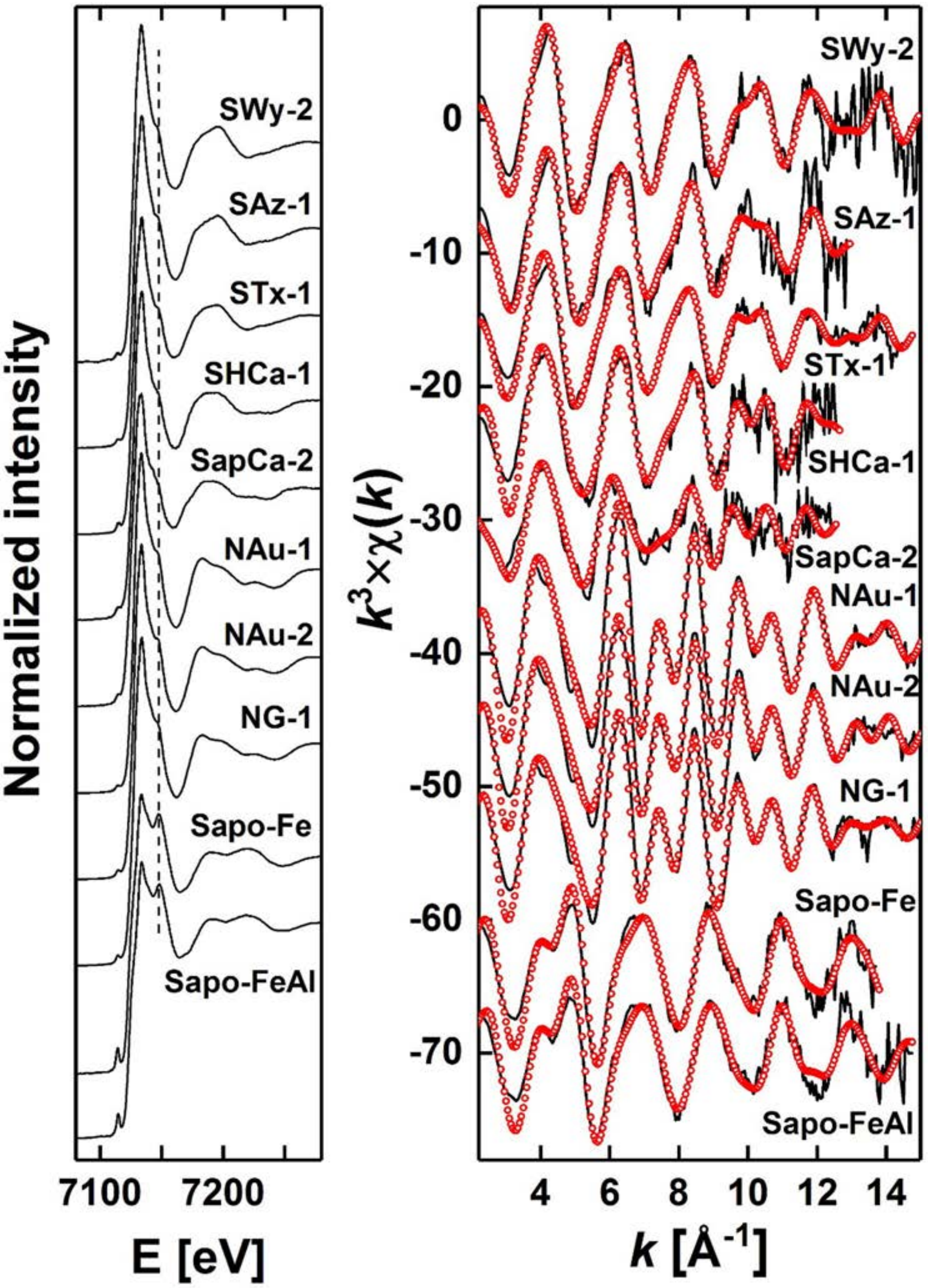

higher amplitude oscillation, especially in the 6–10 Å^{-1} range, than that of montmorillonites, SHCa-1 and SapCa-2. Yet, features at $k \sim 7.5$ and ~ 10 Å^{-1} are present in these latter spectra but are of much lower intensity. These results evidence clear differences in Fe local environment. Sapo-Fe and Sapo-FeAl have similar spectra, but differ from these of all other smectites. They have a lower oscillation frequency with a lower decrease in oscillation amplitude at higher *k* values, and the oscillation split at $k \sim 5$ Å^{-1} is not observed in the other spectra. These results strongly suggest clear differences in Fe local environments and are corroborated by the corresponding FT (Fig. 6). All FT display a first peak at $R + \Delta R \sim 1.6$ Å originating from the O1 shell and higher distance FT peaks corresponding to contributions from nearest octahedral and tetrahedral cationic neighbors and next nearest O shells. Interestingly, the first FT peak in synthetic saponites is slightly narrower than in the natural smectites, and may originate from differences in the coordination geometry (and thus site symmetry) of the absorber. The first FT peak of NG-1 is of slightly lower amplitude compared to NAu-1 and NAu-2, and may possibly be attributed to the coexistence of $^{[6]}$Fe–O and $^{[4]}$Fe–O (Manceau et al. 2000). In

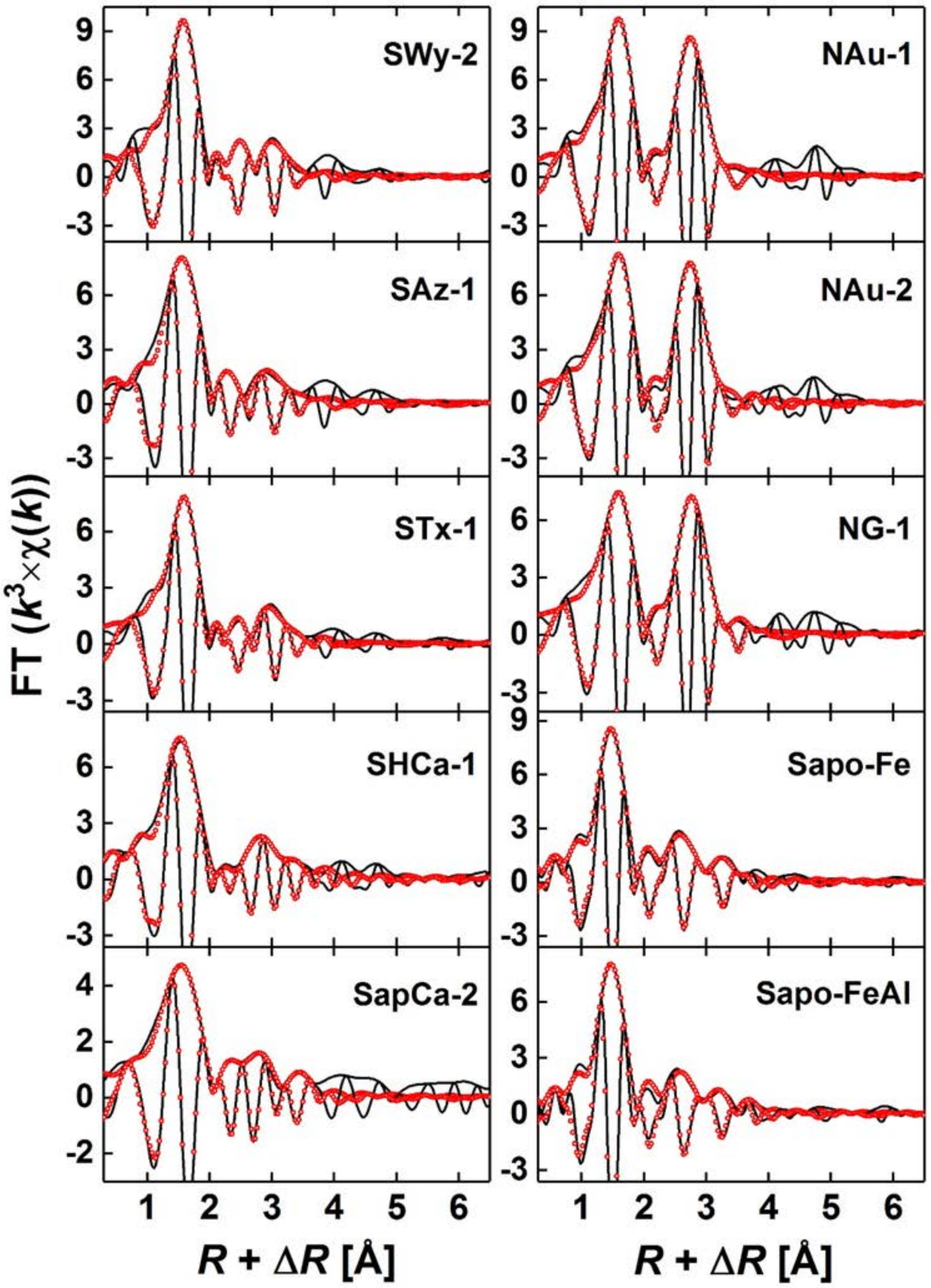

Fig. 6 Experimental (solid black line) and modeled (red symbols) powder ($\alpha = 35°$) Fourier transforms of all smectites. Fit results are presented in Tables 4, 5, 6, and 7

the 2.0–3.5 Å range, the FT of nontronites display a contribution with an amplitude comparable to that of the first FT peak, whereas in all other natural and synthetic smectites, the FT contribution in that range is of much lower amplitude. Furthermore, FT suggest differences in Fe local environment between the synthetic saponites and SapCa-2, and between the trioctahedral smectites and the montmorillonites.

All polarized EXAFS spectra (Figs. 7, 8, 9, 10) exhibit significant angular dependences and contain well-defined isosbestic points attesting to the high degree of particles orientation within the films. The variation in amplitude and position of the oscillation maxima, e.g., at $k \sim 5$ and ~ 6.5 Å^{-1} for the natural smectites and at $k \sim 7$ and ~ 9 Å^{-1} for the synthetic saponites, indicate the presence of atomic shells with distinct orientations. In the polarized FT of all samples (Figs. 7, 8, 9, 10), the amplitude of the peak near 1.6 Å generally decreases with increasing α, hinting at an in-plane orientation. The angular dependence of higher distance shells is more complex and depends on the sample: changes in amplitude associated with shifts in position suggest the presence of several shells overlapping in distance from the absorber, yet having distinct orientation.

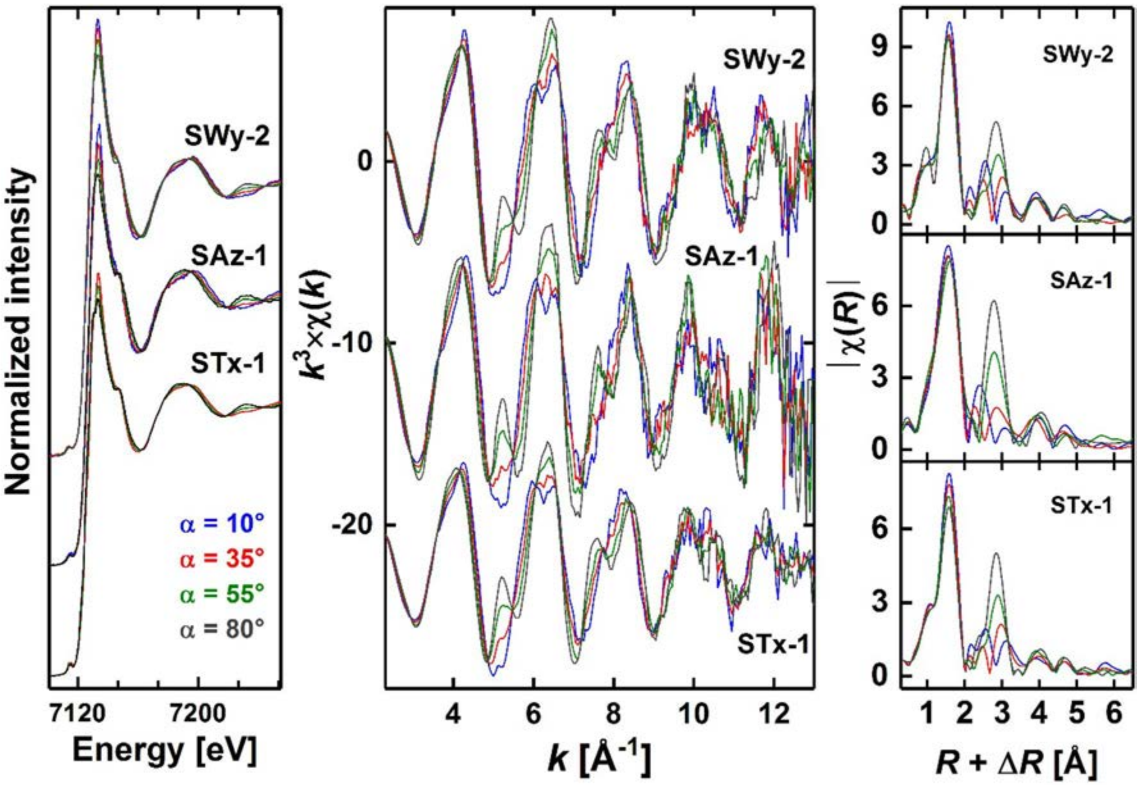

Fig. 7 Experimental Fe *K*-edge polarized XANES (left panel), EXAFS spectra (middle panel), and Fourier transform (right panel) of the montmorillonites. The spectrum of STx-1 at $\alpha = 10°$ was calculated by extrapolation using data recorded at 35°, 55° and 80°

Fig. 8 Experimental Fe *K*-edge polarized XANES (left panel), EXAFS spectra (middle panel), and Fourier transform (right panel) of the nontronites

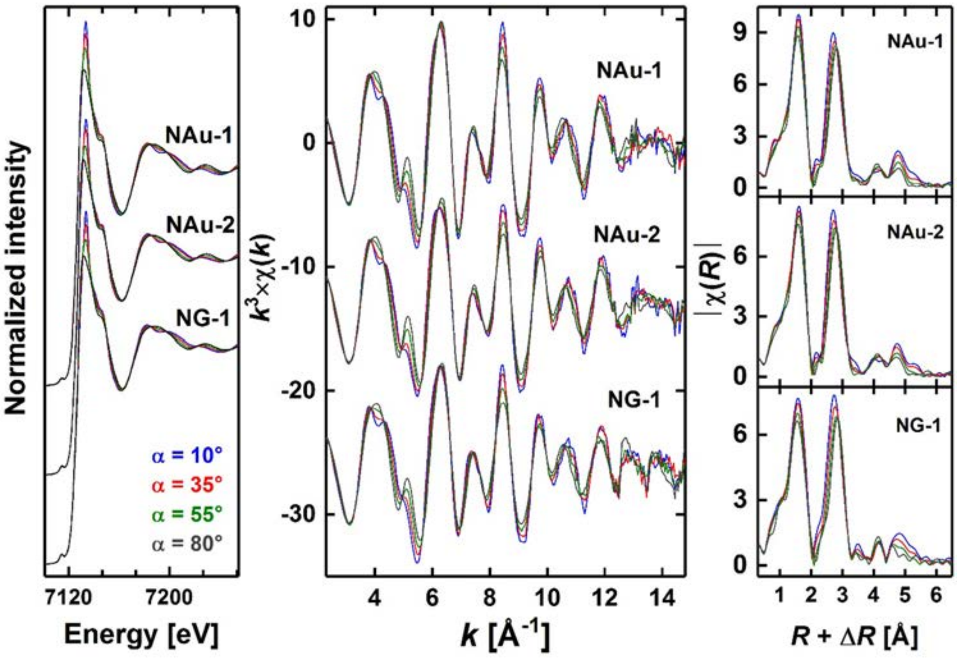

In montmorillonites, the O1 shell was modeled by ~ 6.0 ± 0.5 atoms located at d(Fe–O1) ~ 2.00 Å (Figs. 6, 11; Table 4), matching reported values for octahedral Fe(III) in clay minerals (Finck et al. 2015; Manceau et al. 1998, 2000; Vantelon et al. 2003). The slight decrease in O1 coordination number (N_{O1}) with increasing α values hints

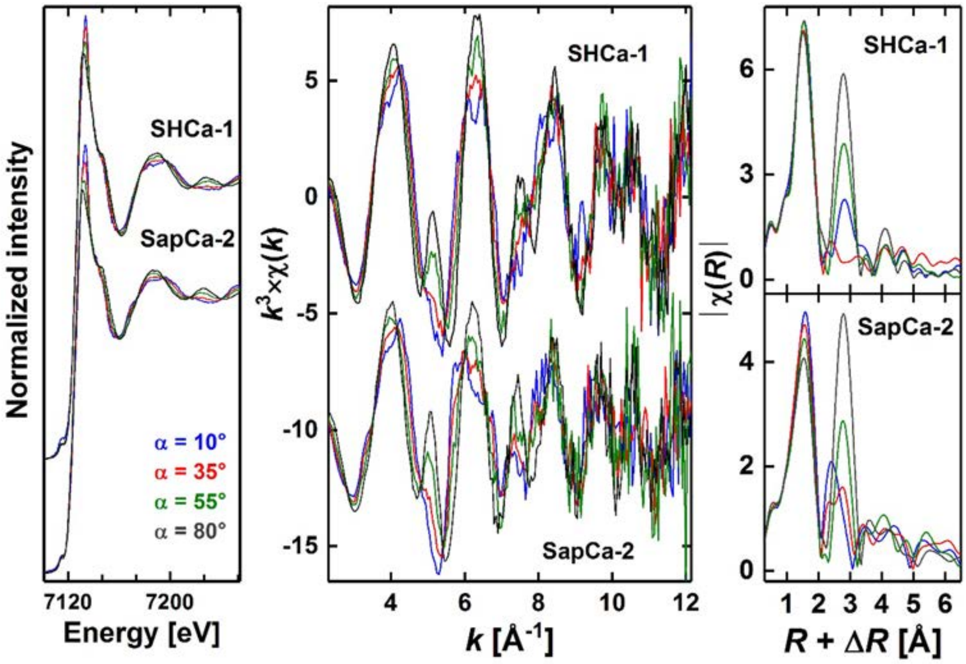

Fig. 9 Experimental Fe *K*-edge polarized XANES (left panel), EXAFS spectra (middle panel), and Fourier transform (right panel) of the hectorite SHCa-1 and the saponite SapCa-2

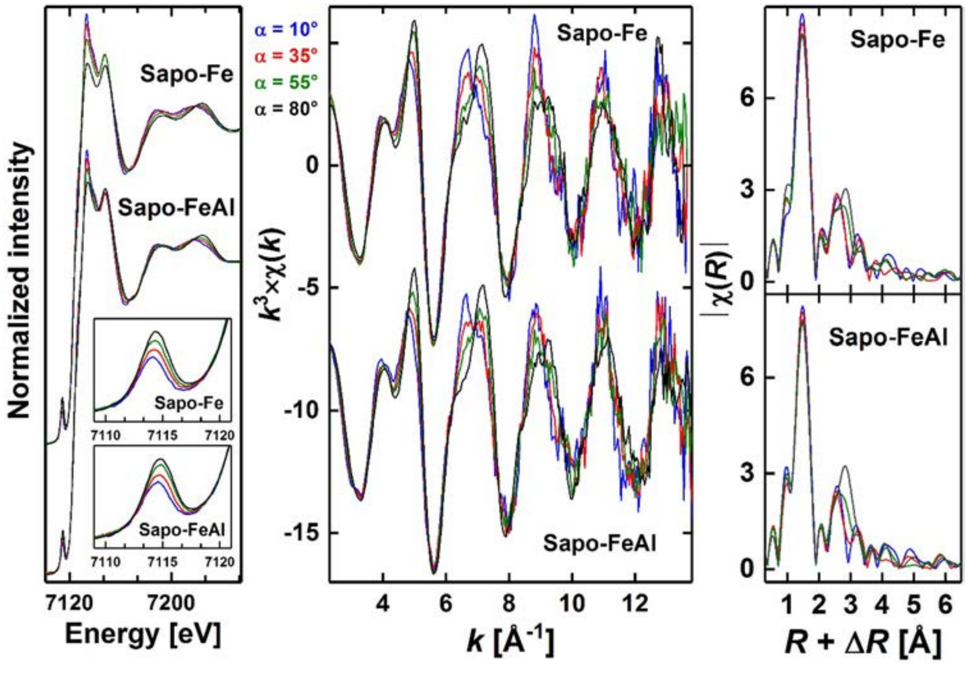

Fig. 10 Experimental Fe *K*-edge polarized XANES (left panel), EXAFS spectra (middle panel), and Fourier transform (right panel) of the synthetic saponites

at an in-plane orientation of the Fe–O1 pair, as expected for Fe located at octahedral position. The observed decrease in apparent coordination number (N^{α}) suggests that the angle (β) between the Fe–O1 vector and the clay layer normal is larger than 54.7°. Variations in N^{α} are linked to α (angle between the electric field of the X-ray beam and the clay layer plane) and β (angle between the absorber–backscatterer pair and the clay layer normal) following (e.g., Manceau 1990; Manceau et al. 1998; Schlegel et al. 1999): $N^{\alpha} = N^{\text{pwdr}}\left(1 - \frac{(3\cos^2\beta-1)(3\cos^2\alpha-2)}{2}\right)$, where N^{pwdr} is the coordination number for a perfectly disordered powder. Consequently, $N^{\alpha} = N^{\text{pwdr}}$ when $\alpha = 35.3°$ regardless of β, and for $\beta = 54.7°$ regardless of α. For octahedral sites in clay minerals, Fe–O pairs are not aligned with the layer plane, but are inclined by 54.7° with respect to the clay normal for fully symmetric octahedra. However, octahedral flattening leads to a slight increase of this angle,

Fig. 11 Experimental (solid black line) and modeled (red symbols) polarized FT at $\alpha = 10°$, 55°, and 80° of the montmorillonites and SHCa-1. Fit results are indicated in Tables 4, 5, and 6. The data of STx-1 at $\alpha = 10°$ were calculated by extrapolation using data recorded at 35°, 55°, and 80°

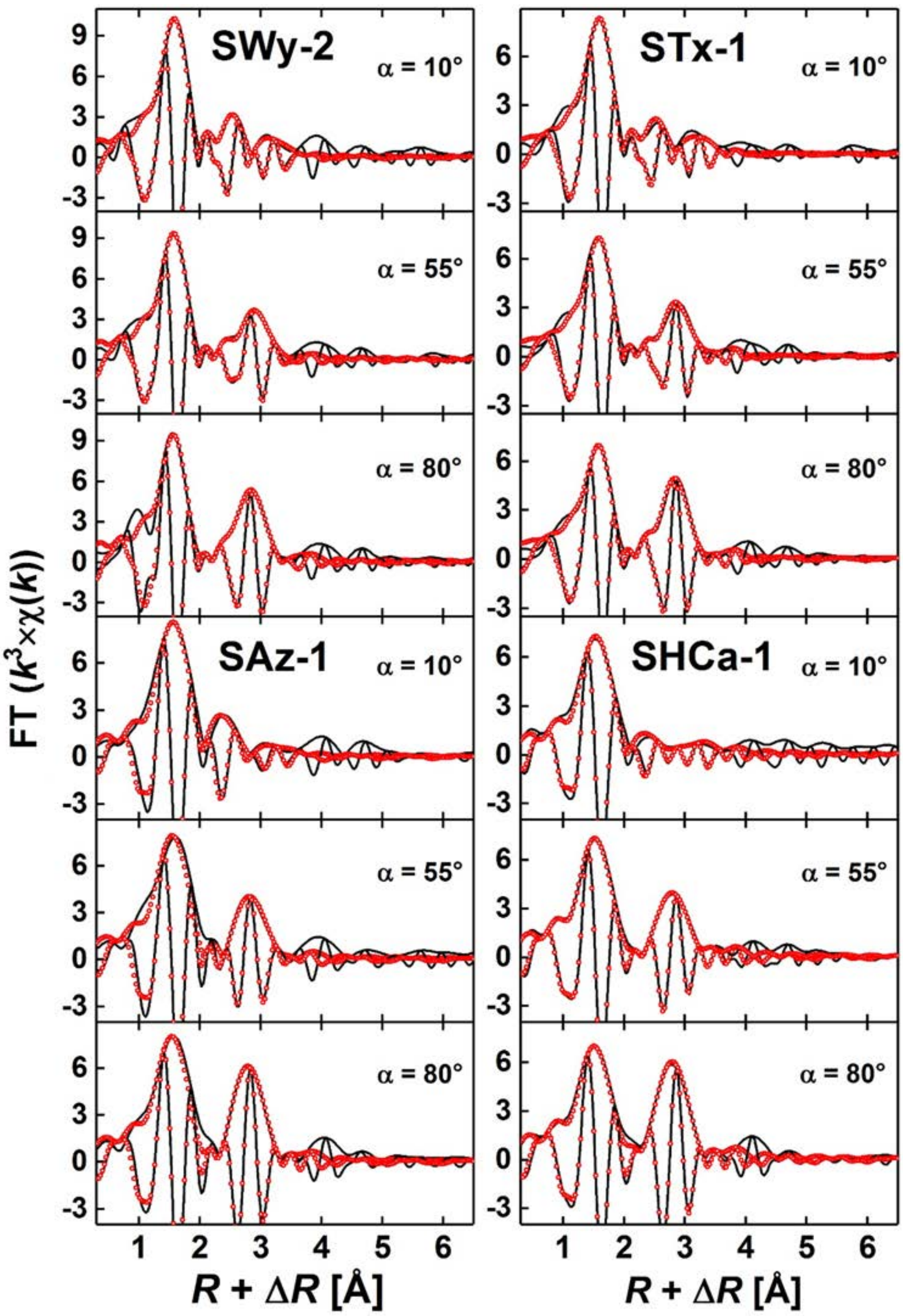

resulting in a slight decrease in the apparent number of O neighbors with increasing α. At higher distances, FT contributions at $R + \Delta R \sim 2.4$ Å and ~ 3.0 Å (Fig. 7) exhibit a complex angular dependence. The amplitude of the contribution centered at ~ 2.4 Å decreases, whereas that centered at 3.0 Å increases, and is shifted to lower distances with increasing α. These dependencies were adequately modeled by assuming Al, Fe, and Si neighbors at d(Fe-Al1) = 3.03–3.06 Å, d(Fe-Fe1) = 3.02–3.07 Å, and d(Fe-Si1) = 3.22–3.24 Å (Table 5). In all three samples, N_{Al1} and N_{Fe1} decrease, whereas N_{Si1} increases with α values, indicating in-plane orientation of Al1 and Fe1 shells and out-of-plane orientation of the Si1 shell. Variations of N_{Si1} and of N_{Al1} with α are remarkably large. For example, at 10°, the number of detected Si1 neighbors for SWy-2 is only half that of the crystal value, whereas at 80°, it is double that value. Using the previous relationship between the apparent and the real value, with $\beta = 32°$ for this shell,

Table 4 Quantitative EXAFS analysis of the first coordination sphere and parameters used for the fits (the O1 shell in NG-1 is split in two subshells, O1a and O1b)

Sample	k range [Å^{-1}]	R range [Å]	α [°]	O1 shell			ΔE_0 [eV]	R_f ($\times 10^3$)
				N	R [Å]	σ^2 [Å^2]		
SWy-2	4.0–11.7	1.3–3.8	10	6.0 (4)	2.00 (2)	0.005	4.4 (4)	13.2
			35	5.6 (4)				
			55	5.5 (3)				
			80	5.5 (3)				
SAz-1	4.0–10.3	1.3–3.8	10	6.0 (5)	2.01 (2)	0.006	6.1 (5)	22.2
			35	5.7 (5)				
			55	5.6 (4)				
			80	5.7 (4)				
STx-1	4.0–12.5	1.3–3.8	10	5.5 (4)	2.01 (2)	0.006	4.4 (5)	12.0
			35	5.2 (3)				
			55	4.8 (4)				
			80	4.6 (4)				
SHCa-1	4.0–10.4	1.3–3.8	10	5.3 (4)	2.00 (2)	0.004	5.3 (7)	9.6
			35	5.5 (3)				
			55	5.4 (3)				
			80	5.2 (4)				
SapCa-2	4.0–9.7	1.3–3.8	10	5.4 (4)	2.01 (2)	0.010	4.4 (7)	10.2
			35	5.2 (3)				
			55	4.8 (4)				
			80	4.5 (3)				
NAu-1	4.0–13.2	1.3–3.8	10	6.2 (4)	2.00 (2)	0.006	5.3 (5)	4.0
			35	6.0 (4)				
			55	5.8 (4)				
			80	5.5 (4)				
NAu-2	4.0–13.2	1.3–3.8	10	5.7 (4)	2.00 (2)	0.006	5.8 (4)	7.7
			35	5.5 (4)				
			55	5.3 (4)				
			80	5.0 (4)				
NG-1	4.0–12.8	1.3–3.8	10	0.6 (2)	1.88 (2)	0.002	5.0 (6)	6.4
			35	0.6 (2)				
			55	0.5 (2)				
			80	0.5 (2)				
			10	5.4 (5)	2.00 (2)	0.005		
			35	5.1 (4)				
			55	4.9 (4)				
			80	4.6 (4)				
Sapo-Fe	4.2–12.0	1.3–3.8	10	3.5 (4)	1.86 (2)	0.003	−0.9 (7)	31.6
			35	3.4 (3)				
			55	3.2 (3)				
			80	3.0 (3)				
Sapo-FeAl	4.2–12.0	1.3–3.8	10	3.3 (4)	1.86 (2)	0.003	−0.5 (6)	37.1
			35	3.2 (3)				
			55	3.1 (4)				
			80	3.0 (4)				

Data were modeled over the entire range considering data from this table and that from Tables 5, 6, and 7. Uncertainties on coordination numbers and bond distances are indicated in parentheses, and the fit quality is quantified by the R_f factor representing the absolute misfit between theory and data

Table 5 Quantitative EXAFS analysis of higher distance atomic shells for montmorillonites and nontronites

Sample	α [°]	Al1 shell			Fe1 shell			Si1 shell			O2 shell			O3 shell		
		N	R [Å]	σ^2 [Å^2]	N	R [Å]	σ^2 [Å^2]	N	R [Å]	σ^2 [Å^2]	N	R [Å]	σ^2 [Å^2]	N	R [Å]	σ^2 [Å^2]
SWy-2	10	3.2 (8)	3.05 (2)	0.004	0.3 (2)	3.05 (3)	0.007	2.2 (12)	3.22 (2)	0.008	5.0 (23)	3.75 (4)	0.007	0.6 (30)	3.95 (5)	0.007
	35	2.7 (4)			0.3 (2)			4.1 (7)			5.8 (6)			2.7 (20)		
	55	1.6 (7)			0.2 (2)			6.1 (10)			6.4 (5)			4.7 (20)		
	80	0.8 (5)			0.1 (2)			7.7 (7)			6.5 (17)			7.1 (20)		
SAz-1	10	3.7 (4)	3.03 (2)	0.006	0.3 (2)	3.02 (3)	0.005	1.3 (5)	3.23 (3)	0.007	3.2 (6)	3.80 (4)	0.009	0.1 (8)	4.00 (4)	0.007
	35	2.8 (3)			0.2 (2)			3.4 (4)			3.7 (8)			0.4 (29)		
	55	1.3 (3)			0.1 (2)			5.6 (7)			4.5 (36)			3.0 (35)		
	80	0.3 (4)			0.0 (1)			7.7 (6)			5.2 (36)			5.5 (32)		
STx-1	10	2.1 (5)	3.06 (2)	0.004	0.3 (2)	3.07 (2)	0.005	1.2 (4)	3.24 (3)	0.008	4.8 (6)	3.77 (4)	0.007	2.1 (19)	3.98 (5)	0.009
	35	1.9 (4)			0.2 (2)			3.8 (3)			4.7 (13)			3.0 (17)		
	55	0.9 (4)			0.1 (1)			5.4 (3)			4.5 (13)			5.1 (17)		
	80	1.0 (3)			0.1 (2)			8.0 (5)			4.6 (5)			5.8 (11)		
NAu-1	10	–	–	–	3.6 (4)	3.06 (2)	0.005	2.3 (6)	3.26 (2)	0.007	7.7 (14)	3.75 (4)	0.008	3.5 (13)	3.90 (5)	0.007
	35				2.8 (3)			4.0 (3)			5.5 (12)			3.8 (11)		
	55				1.7 (2)			6.2 (6)			3.8 (13)			4.2 (11)		
	80				0.8 (4)			7.9 (7)			1.8 (15)			4.8 (12)		
NAu-2	10	–	–	–	3.6 (3)	3.07 (2)	0.005	1.8 (7)	3.25 (2)	0.008	6.8 (20)	3.74 (4)	0.007	3.3 (23)	3.92 (5)	0.007
	35				2.7 (2)			3.9 (3)			6.2 (13)			3.6 (16)		
	55				1.9 (3)			6.0 (6)			4.4 (13)			4.0 (14)		
	80				1.1 (4)			8.0 (6)			3.0 (13)			4.5 (13)		
NG-1	10	–	–	–	3.5 (3)	3.07 (2)	0.006	2.7 (6)	3.26 (2)	0.006	5.3 (12)	3.69 (4)	0.006	6.2 (15)	3.86 (5)	0.007
	35				2.5 (3)			4.1 (3)			3.6 (9)			5.3 (10)		
	55				1.4 (3)			5.6 (6)			2.0 (11)			4.5 (12)		
	80				0.4 (3)			6.9 (5)			0.2 (4)			3.5 (10)		

Data were modeled over the entire range considering data from this table and from Table 4. Uncertainties on coordination numbers and bond distances are indicated in parentheses, and the fit quality is quantified by the R_f factor representing the absolute misfit between theory and data the apparent coordination numbers at these two angles can be written $N_{\mathrm{Si}}^{10} = N_{\mathrm{Si}}^{\mathrm{pwdr}}\left(1 - \frac{(3\cos^2(32)-1)(3\cos^2(10)-2)}{2}\right)$ and $N_{\mathrm{Si}}^{80} = N_{\mathrm{Si}}^{\mathrm{pwdr}}\left(1 - \frac{(3\cos^2(32)-1)(3\cos^2(80)-2)}{2}\right)$, respectively. Because octahedral cations in smectites are surrounded by four tetrahedral cationic neighbors (i.e., $N_{\mathrm{Si}}^{\mathrm{pwdr}} = 4$), calculations yield $N_{\mathrm{Si}}^{10} = 1.9$ and $N_{\mathrm{Si}}^{80} = 8.4$. The calculated values match within uncertainties experimental values (Table 5), providing thereby further strong evidence about the successful preparation of highly oriented clay films. In SWy-2 and SAz-1, the number of octahedral neighbors (Al + Fe) at $\alpha = 35°$ equals 3, in agreement with a dioctahedral framework, whereas it is slightly lower in STx-1. The number of neighboring Si is close to 4 in all montmorillonites, in agreement with the crystal structure. At higher distances, fits were improved using O shells at distances close to reported values and originating from adjacent octahedra (O2 shell) and from the basal planes (O3 shell). For SWy-2 and STx-1, N_{O2} and N_{O3} at $\alpha = 35°$ are reasonably close to reported crystallographic values ($N_{\mathrm{O2}} = 6$ and $N_{\mathrm{O3}} = 4$; Tsipursky and Drits 1984), and shells are oriented out-of-plane. For SAz-1, N_{O2} and N_{O3} are low and N_{O2} seems not affected by α variations. SAz-1 has a higher octahedral layer charge than SWy-2 and STx-1, which may cause increased structural disorder and result in dampening of EXAFS contributions and weakening of angular dependences for distant shells. For all montmorillonites, the low number of detected Fe–Fe pairs excludes extensive clustering. These results contrast with the Fe clustering reported for SAz-1 and STx-1, yet they are in agreement with the Fe exclusion rule for SWy-2 (Vantelon et al. 2003). Differences may reside in the better ability of polarized EXAFS compared to powder EXAFS to filter out overlapping contributions from shells with distinct orientations, thereby reducing uncertainties on structural parameters.

The O1 shell in SHCa-1 and SapCa-2 consists of 5–6 atoms oriented in-plane and located at d(Fe–O1) ~ 2.00 Å (Figs. 6, 11, 12; Table 4). The FT of both samples display high amplitude contributions at higher distance, but with contrasted angular behaviors. The amplitude of the FT contribution at $R + \Delta R \sim 2.8$ Å increases with α and the position hardly varies in SHCa-1, in agreement with earlier findings (Finck et al. 2015). In SapCa-2, the amplitude of the FT contribution at $R + \Delta R \sim 2.4$ Å decreases, whereas that at ~ 2.8 Å increases with α. In both smectites, these contributions were modeled considering neighboring octahedral Mg [d(Fe–Mg1) = 3.05–3.08 Å] and Fe [d(Fe–Fe1) = 3.04–3.08 Å], and tetrahedral Si [d(Fe–Si1) = 3.25–3.28 Å] atoms (Table 6). In both samples, N_{Si1} matches expectations for tetrahedral neighbors, but the number of detected octahedral neighbors (Mg + Fe) is low compared to the expected structural value of 6. Several explanations can account for this discrepancy. First, neighboring Fe may be substituted by a combination of Al and Mg atoms, implying that the local environment would not correspond to a pure trioctahedral framework but to a mixed trioctahedral–dioctahedral one. Similarly, the increased local charge resulting from Fe(III) substitution for Mg(II) may be compensated by vacant adjacent octahedral sites, and in SHCa-1 by preferential Li(I) insertion, which would result in a low number of octahedral cations (Finck et al. 2015). Another hypothesis would be destructive interferences between electronic waves backscattered by octahedral Fe and Mg/Al neighbors (Manceau 1990) which would lower the actual number of detected atoms. Finally, a preferential location of Fe octahedra at platelet edges would as well limit the number of neighboring octahedral cations. Note that deprotonation of hydroxyl groups and substitution of $^{[4]}$Al for $^{[4]}$Si are other possible charge balance mechanisms. For both smectites, fits were improved by including an O shell at d(Fe–O_2) = 3.34–3.44 Å with a coordination number close to reported crystallographic values ($N_{\mathrm{O2}} = 2$; Breu et al. 2003). This shell corresponds to O atoms from the basal planes and was not detected in montmorillonites because of corrugation of the basal oxygen planes (Manceau et al. 2000). Finally, additional in-plane (O_3) and out-of-plane (O_4) O shells were detected at d(Fe–O_3) ~ 3.70 Å and d(Fe–O_4) ~ 4.00 Å, and correspond to the same shells as in montmorillonites.

The FT of the nontronites contain two high amplitude contributions at $R + \Delta R \sim 1.6$ Å and ~ 2.8 Å (Fig. 8). In NAu-1 and NAu-2, the O1 shell contains 6 atoms oriented in-plane (Figs. 6, 12; Table 4), whereas in NG-1, it is split into two subshells containing 0.6(2) and 5.1(4) atoms at d(Fe–O1a) = 1.88(2) Å and d(Fe–O1b) = 2.00(2) Å, respectively. Based on reported data, the O1a shell corresponds to $^{[4]}\mathrm{Fe}^{3+}$, and coordination numbers indicate that 15% of Fe is located in the tetrahedral sheet (Gates et al. 2002; Manceau et al. 2000). The absence of $^{[4]}\mathrm{Fe}^{3+}$ in NAu-1 and NAu-2 also compares with earlier findings showing the presence of ~ 2% of total Fe^{3+} within the tetrahedral sheet of NAu-1 and up to ~ 7.5% in NAu-2 (Gates et al. 2002). These reported amounts are within the detection limit of EXAFS spectroscopy, and thus including an additional Fe^{3+} shell would not significantly improve the fit. For all nontronites, the amplitude of the FT contribution at $R + \Delta R \sim 2.8$ Å decreases and is shifted to higher distances for increasing α values, indicating the presence of more than one shell. Neighboring in-plane Fe and out-of-plane Si shells were detected at d(Fe–Fe1) = 3.06–3.07 Å and d(Fe–Si1) = 3.25–3.26 Å (Table 5), respectively, with coordination numbers matching expectations for octahedral and tetrahedral neighbors. As for montmorillonites, two additional O shells were used to improve FT modeling at higher distances. In NAu-1 and NAu-2, these shells consist in six in-plane and four out-of-plane O atoms, respectively. Similar shells were detected in

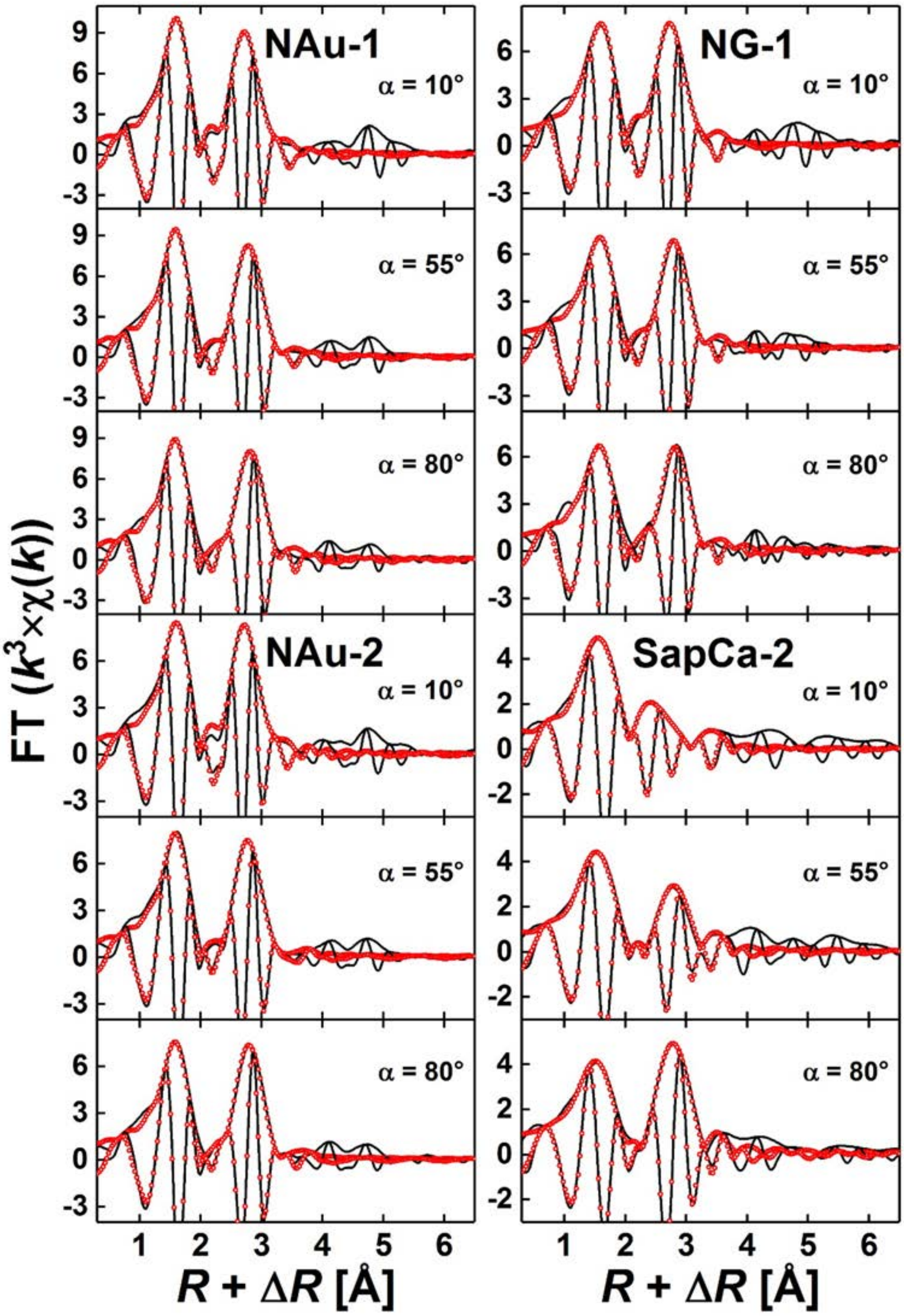

Fig. 12 Experimental (solid black line) and modeled (red symbols) polarized FT at $\alpha = 10°$, 55°, and 80° of the nontronites and SapCa-2. Fit results are indicated in Tables 4, 5, and 6

NG-1, but N_{O2} and N_{O3} slightly differ certainly as a consequence of Fe distribution in two distinct environments. Note that the FT of all nontronites contains peaks exhibiting angular dependence up to $R + \Delta R \sim 5.5$ Å; however, no attempt was made to model these long-distance contributions.

The FT of Sapo-Fe and Sapo-FeAl contain a first peak at slightly shorter distance ($R + \Delta R \sim 1.5$ Å) than in the other samples (Fig. 6), and the contribution centered around $R + \Delta R \sim 2.8$ Å exhibits a complex angular dependence (Fig. 10). The low distance side of the latter contribution slightly decreases, whereas the high distance side increases hinting at contributions of overlapping shells of distinctively different orientations. In both samples, the first FT peak was modeled with ~ 3 O atoms at d(Fe–O1) = 1.86(2) Å (Figs. 6, 13; Table 4). This bond length indicates a tetrahedral coordination, and the increase in length from d(Si–O) = 1.62 Å to d(Fe–O1) matches the increase in size from $^{[4]}Si^{4+}$ ($r = 0.26$ Å) to

Table 6 Quantitative EXAFS analysis of higher distance atomic shells for the hectorite SHCa-1 and the saponite SapCa-2

α [°]	Mg1 shell			Fe1 shell			Si1 shell			O2 shell			O3 shell			O4 shell		
	N	R [Å]	σ^2 [Å^2]	N	R [Å]	σ^2 [Å^2]	N	R [Å]	σ^2 [Å^2]	N	R [Å]	σ^2 [Å^2]	N	R [Å]	σ^2 [Å^2]	N	R [Å]	σ^2 [Å^2]
SHCa-1																		
10	2.5 (3)	3.08 (2)	0.006	0.3 (2)	3.08 (3)	0.008	2.6 (3)	3.25 (2)	0.007	0.4 (4)	3.44 (4)	0.006	6.1 (13)	3.70 (4)	0.007	2.6 (8)	3.95 (5)	0.007
35	1.6 (4)			0.2 (2)			4.2 (4)			1.8 (4)			7.5 (22)			3.2 (25)		
55	0.2 (12)			0.0 (2)			4.7 (14)			2.9 (3)			5.6 (30)			4.1 (33)		
80	0.1 (3)			0.0 (2)			7.1 (4)			3.5 (4)			4.1 (8)			4.4 (15)		
SapCa-2																		
10	3.2 (3)	3.05 (2)	0.006	0.1 (2)	3.04 (4)	0.005	2.0 (4)	3.28 (2)	0.008	0.7 (3)	3.34 (3)	0.005	2.7 (8)	3.70 (5)	0.005	1.6 (15)	4.13 (5)	0.008
35	2.7 (3)			0.1 (2)			3.9 (3)			1.4 (4)			2.3 (6)			2.1 (7)		
55	1.3 (3)			0.1 (2)			5.4 (8)			1.7 (3)			0.9 (7)			2.7 (8)		
80	0.8 (4)			0.1 (2)			8.6 (7)			2.1 (4)			0.2 (6)			3.3 (17)		

Data were modeled over the entire range considering data from this table and from Table 4. Uncertainties on coordination numbers and bond distances are indicated in parentheses, and the fit quality is quantified by the R_f factor representing the absolute misfit between theory and data

$^{[4]}Fe^{3+}$ ($r = 0.49$ Å) (Shannon 1976). N_{O1} at $\alpha = 35°$ is slightly lower than the theoretical coordination number of four and exhibits weak angular dependence. For Fe located in the tetrahedral sheet, three O atoms are distributed in one plane parallel to the *ab* axis [basal O atoms (O_{basal})] and the fourth atom [apical O (O_{apical})] is shared with the octahedral sheet. Furthermore, the Fe–O_{apical} vector is perpendicular to the layer plane, whereas the Fe–O_{basal} vector is inclined by 70° with respected to the plane normal. Insight into the weak angular dependence of N_{O1} can be obtained using the relationship between the apparent and the real coordination number. Because the orientation of the Fe–O_{basal} vector differs substantially from the Fe–O_{apical} vector, the O1 shell can be split into two subshells for calculations, O_{apical} with $\beta = 180°$ and O_{basal} with $\beta = 70°$. At $\alpha = 10°$ and 80°, calculated apparent coordination numbers of these subshells are $N^{10}_{\text{Oapical}} = N^{\text{pwdr}}_{\text{Oapical}}\left(1 - \frac{(3\cos^2(180)-1)(3\cos^2(10)-2)}{2}\right) = 0.1$ and $N^{80}_{\text{Oapical}} = N^{\text{pwdr}}_{\text{Oapical}}\left(1 - \frac{(3\cos^2(180)-1)(3\cos^2(80)-2)}{2}\right) = 2.9$, and $N^{10}_{\text{Obasal}} = N^{\text{pwdr}}_{\text{Obasal}}\left(1 - \frac{(3\cos^2(70)-1)(3\cos^2(10)-2)}{2}\right) = 3.9$ and $N^{80}_{\text{Obasal}} = N^{\text{pwdr}}_{\text{Obasal}}\left(1 - \frac{(3\cos^2(70)-1)(3\cos^2(80)-2)}{2}\right) = 1.1$, respectively. Consequently, for the O1 shell, the apparent coordination number at $\alpha = 10°$ ($3.9 + 0.1 = 4.0$) equals that at $\alpha = 80°$ ($1.1 + 2.9 = 4.0$), which is also equal to the crystallographic value. This finding implies that this shell should not exhibit any angular dependence, and experimental data corroborate these calculations. The observed weak angular dependence can easily be accounted for by a shift of Fe atoms from regular position of tetrahedral cations within the structure as a consequence of structural strain induced by accommodation of this large cation. Furthermore, the $^{[4]}$Fe for $^{[4]}$Si substitution results in an increase of the dimension of the tetrahedral sheet, thereby increasing the size mismatch with the octahedral sheet, and a rotation of adjacent tetrahedra around the layer normal compensates this misfit. Note that this structural strain also leads to a significant dispersion of the individual Fe–O1 distances (Manceau et al. 2000), resulting in a number of detected O1 atoms lower than the crystallographic value of 4. In-plane Si (d(Fe–Si1) = 3.18–3.20 Å) and out-of-plane Mg (d(Fe–Mg1) = 3.33–3.34 Å) atoms were detected (Table 7) at distances larger than d(Si–Si) = 3.03 Å and d(Si–Mg) = 3.18 Å in saponite, and is attributed to the larger size of $^{[4]}Fe^{3+}$ compared to $^{[4]}$Si. An Fe shell was also detected at d(Fe–Fe1) = 3.24–3.25 Å originating from substitution for $^{[4]}$Si, but the low N_{Fe1} (≤ 0.3) excludes clustering. In both samples, the number of detected tetrahedral neighbors ($N_{Si1} + N_{Fe1}$) matches the number of neighboring cations in a tetrahedral sheet. Additional O shells originating from neighboring octahedra (O2 shell at ~3.56 Å) and from neighboring tetrahedra (O3 shell at

Fig. 13 Experimental (solid black line) and modeled (red symbols) polarized FT at $\alpha = 10°$, 55°, and 80° of the synthetic saponites. Fit results are indicated in Tables 4 and 7

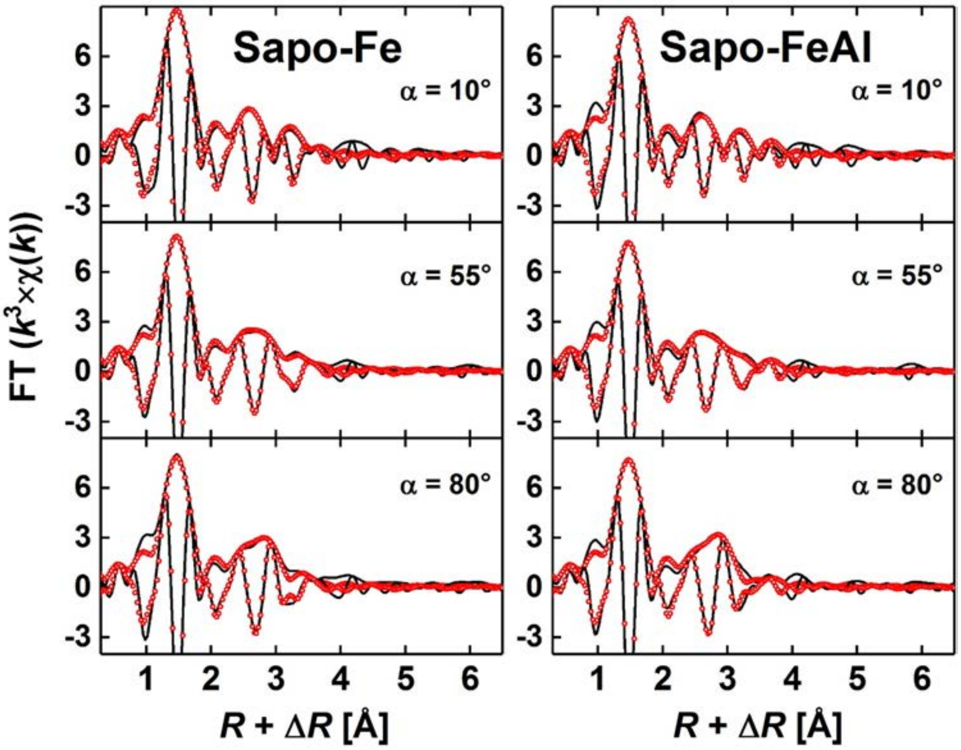

Table 7 Quantitative EXAFS analysis of higher distance atomic shells for the synthetic saponites Sapo-Fe and Sapo-FeAl

α [°]	Si1 shell			Fe1 shell			Mg1 shell			O2 shell			O3 shell		
	N	*R* [Å]	σ^2 [Å^2]	*N*	*R* [Å]	σ^2 [Å^2]	*N*	*R* [Å]	σ^2 [Å^2]	*N*	*R* [Å]	σ^2 [Å^2]	*N*	*R* [Å]	σ^2 [Å^2]
Sapo-Fe															
10	3.2 (3)	3.18 (2)	0.003	0.3 (2)	3.24 (3)	0.003	5.8 (11)	3.33 (3)	0.004	7.8 (19)	3.57 (4)	0.005	2.9 (7)	4.04 (6)	0.006
35	2.8 (3)			0.2 (2)			6.2 (9)			7.1 (15)			2.6 (12)		
55	2.2 (4)			0.2 (2)			6.5 (8)			5.7 (15)			3.0 (7)		
80	2.0 (3)			0.2 (3)			7.0 (7)			4.8 (12)			2.9 (8)		
Sapo-FeAl															
10	3.1 (4)	3.20 (2)	0.003	0.4 (2)	3.25 (4)	0.002	3.8 (9)	3.34 (3)	0.003	6.3 (8)	3.56 (3)	0.005	3.3 (7)	4.09 (6)	0.006
35	2.7 (3)			0.3 (2)			4.3 (7)			6.2 (6)			3.0 (5)		
55	2.4 (3)			0.3 (2)			5.1 (7)			5.6 (14)			3.1 (4)		
80	2.1 (3)			0.3 (3)			6.1 (8)			4.6 (11)			2.8 (15)		

Data were modeled over the entire range considering data from this table and from Table 4. Uncertainties on coordination numbers and bond distances are indicated in parentheses, and the fit quality is quantified by the R_f factor representing the absolute misfit between theory and data

~4.05 Å), were used to improve fits at higher distances. No octahedral Fe could be detected in these saponites.

Discussion

Structural formulae were calculated taking into account clay chemical compositions and spectroscopic results (Table 8). In a first step, Mg is placed in the octahedral sheet and Si in the tetrahedral sheet; in a second step, Al and Fe are distributed among octahedral and tetrahedral sites taking into account MAS-NMR and XAS results, respectively. Calculated formulae show that the investigated smectites have various octahedral filling patterns and different charge locations (Table 8). The distribution and origin of the layer charge between the tetrahedral and octahedral sheets vary from sample to sample, and is always fully balanced by interlayer cations. The origin of layer charge in montmorillonites is almost exclusively $^{[6]}Mg^{2+}$ and increases in the order SWy-2 < STx-1 < SAz-1, and

Table 8 Unit cell formulae of the smectites calculated using results from chemical analyses and spectroscopic results from this work*

Sample	Cation composition per $O_{10}(OH)_2$*	Net tetrahedral charge	Net octahedral charge
SWy-2[a]	$(Si_{3.87}Al_{0.13})(Al_{1.54}Fe^{3+}_{0.21}Mg_{0.25})Na_{0.35}$	−0.13	−0.25
SAz-1[a]	$(Si_{3.98}Al_{0.02})(Al_{1.37}Fe^{3+}_{0.08}Ti_{0.01}Mg_{0.57})Na_{0.47}$	−0.02	−0.47
STx-1[a]	$(Si_{3.99}Al_{0.01})(Al_{1.54}Fe^{3+}_{0.06}Ti_{0.01}Mg_{0.38})Na_{0.40}$	−0.01	−0.40
SHCa-1[b]	$(Si_{3.97}Al_{0.03})(Al_{0.01}Fe^{3+}_{0.01}Mg_{2.65}Li_{0.32})Na_{0.32}K_{0.01}$	−0.03	−0.32
SapCa-2[c]	$(Si_{3.63}Al_{0.37})(Al_{0.01}Fe^{3+}_{0.06}Mg_{2.89})Na_{0.35}Ca_{0.01}$	−0.37	−0.01
NAu-1[d]	$(Si_{3.49}Al_{0.51})(Al_{0.16}Fe^{3+}_{1.82}Mg_{0.02})Na_{0.50}$	−0.51	−0.02
NAu-2[d]	$(Si_{3.80}Al_{0.20})(Al_{0.05}Fe^{3+}_{1.88}Mg_{0.02})Na_{0.35}$	−0.20	−0.17
NG-1[d]	$(Si_{3.62}Al_{0.08}Fe_{0.30})(Al_{0.16}Fe^{3+}_{1.73}Mg_{0.05})Na_{0.65}$	−0.38	−0.23
Sapo-Fe[c]	$(Si_{3.40}Fe_{0.60})(Mg_{3.00})Na_{0.60}$	−0.60	0
Sapo-FeAl[c]	$(Si_{3.40}Al_{0.20}Fe_{0.40})(Mg_{3.00})Na_{0.60}$	−0.60	0

*Sample SHCa-1 contains ~ 3 wt% –F substituting for –OH groups (Thomas et al. 1977). NAu-1 and NAu-2 do not contain tetrahedral Fe, as indicated by polarized EXAFS spectroscopy

[a] Montmorillonite

[b] Hectorite

[c] Saponite

[d] Nontronite

MAS-NMR data exclude extensive $^{[4]}Al^{3+}$ for $^{[4]}Si$ substitution. Calculated formulae for SWy-2 and SAz-1 are in relatively good agreement with reported data of Mermut and Cano (2001). In nontronites, the source of layer charge is $^{[4]}Al^{3+}$, except in NG-1 which contains low amounts of $^{[4]}Fe^{3+}$. The calculated formulae of NAu-1 agrees well with that of Gates et al. (2002) and Keeling et al. (2000). For NAu-2, small discrepancies exist with reported compositions: experimental results evidence the presence of low amounts of octahedral Al^{3+}, whereas Keeling et al. (2000) concluded on its absence and Gates et al. (2002) reported larger amounts than in the present study. Manceau et al. (2000) and Gates et al. (2002) reported relatively comparable structural formula for NG-1, with slightly lower octahedral Fe and slightly higher octahedral Al content than determined in the present study. For the trioctahedral smectites, MAS-NMR data show preferential Al insertion in the tetrahedral sheet, 77% of $^{[4]}Al$ in SHCa-1 and ~ 100% $^{[4]}Al$ in SapCa-2. In SHCa-1, the origin of layer charge is $^{[6]}Li^{+}$, there is only limited $^{[4]}Al$ for $^{[4]}Si$ substitution because of low Al content. In contrast, $^{[4]}Al^{3+}$ and vacancies result in layer charge in SapCa-2. The synthetic saponites have a rather high layer charge originating from $^{[4]}Fe$ substituting for $^{[4]}Si$ (Sapo-Fe) or from $^{[4]}Fe + ^{[4]}Al$ substituting for $^{[4]}Si$ (Sapo-FeAl). Note that experimental data hint at the presence of Fe(III) in all natural samples, but concomitance of Fe(II) below the detection limit of XAS cannot be excluded.

The actual distribution of cations in the octahedral and tetrahedral sheets can be deduced by combining results from IR and EXAFS spectroscopies. Infrared spectroscopy is useful to probe the structural composition of the octahedral sheet, because all OH-sharing cation pairs contribute to the spectrum (Gates 2008). This technique also has no atomic selectivity, meaning that all combinations of cations can be detected. Specifically, the vibrational frequency of the OH-bending band is dependent on the mass of the cations bound to the hydroxyl group. In contrast, EXAFS is element-specific and neighboring atoms such as Mg and Al or Al and Si cannot be discriminated because of similar backscattering phase shifts and amplitudes. Because the *ab* crystallographic planes of individuals platelets are distributed at random in the film plane, EXAFS spectroscopy also cannot provide information on the individual contributions of the Fe–Oct pairs for the in-plane crystallographic orientations. The number of detected Fe, Al, Mg octahedral neighbors corresponds to average values for Fe located at all possible positions. However, comparing the number of detected cationic neighbors with values expected from structural formula can inform on either statistical or preferential (clustering or exclusion) distribution. IR and EXAFS spectroscopies are thus complementary and very useful techniques for investigating the actual distribution of cations in clay minerals. In addition to these techniques, MAS-NMR was also applied in this study to determine the extent of $^{[4]}Al^{3+}$ for $^{[4]}Si$ substitution.

The layer charge in SWy-2, SAz-1, and STx-1 arises predominantly from substitution within the octahedral sheet. The in-plane orientation of neighboring octahedral and out-of-plane orientation of tetrahedral cationic shells hint at the presence of octahedral Fe^{3+}, which fill 3–10% of octahedral sites, and no tetrahedral Fe^{3+} could be detected. Iron clustering is ruled out by the low numbers of neighboring Fe detected by EXAFS spectroscopy ($N_{Fe1} = 0.2–0.3$, Table 5) and by the absence of $Fe^{3+}{}_2$–OH–bending band in the IR spectra (Fig. 3). Additional information on distribution of cations within structural sites can be obtained from the comparison of the intensity of the IR bands in the OH-bending region. Sample SAz-1 has the highest Mg content, and an Fe content comparable to that of STx-1 but lower than in SWy-2. Furthermore, SAz-1 has the $Al^{3+}Mg^{2+}$–OH-bending band of the highest intensity and a low intensity $Fe^{3+}Mg^{2+}$–OH-bending band, thereby suggesting a tendency of Mg to form pairs with Al rather than with Fe. Because of the overlap with opal the intensity of the $Fe^{3+}Mg^{2+}$–OH-bending band cannot be estimated in STx-1, but it may very likely be lower than in SWy-2 because of differences in the Fe content, implying that this latter has the $Fe^{3+}Mg^{2+}$–OH-bending band of highest intensity among montmorillonites. SWy-2 also has an $Fe^{3+}Al^{2+}$–OH-bending band of low intensity, suggesting that Fe^{3+} has a tendency to form pairs with Mg rather than with Al. The presence of cristobalite-like impurities in STx-1 hinders the comparison of the intensity of the $Fe^{3+}Mg^{2+}$–OH and $Al^{3+}Mg^{2+}$–OH-bending bands, and thus any conclusion on possible tendency to form pairs in the octahedral sheet.

In trioctahedral SHCa-1 and SapCa-2, the layer charge originates almost exclusively from substitutions within the octahedral or the tetrahedral sheets, respectively. Based on structural formulae, hydroxyl groups in SapCa-2 are almost exclusively bound to three Mg atoms, whereas they can also be bound to Li in SHCa-1, because about 10% of octahedral sites are filled with Li^+. The FTIR spectra of SHCa-1 and SapCa-2 (Fig. 3) contain an $Fe^{3+}Mg^{2+}$–OH-bending band but no $Fe^{3+}Al^{3+}$–OH contribution, in agreement with MAS-NMR results, implying that Fe may only form pairs with Mg. The intensity of the $Fe^{3+}Mg^{2+}$–OH-bending band correlates with the Fe content and with the number of detected neighboring Mg atoms by EXAFS spectroscopy (Table 8). Both samples have a very low Fe content, and calculations for SHCa-1 ($0.01/3 = 0.003$) and SapCa-2 ($0.06/3 = 0.02$) indicate that at maximum 2% of octahedral sites are filled with Fe. In trioctahedral smectites, each octahedral cation has six octahedral neighbors, and thus for fully random distribution within the octahedral sheet < 0.1 (0.003×6) or 0.1 (0.02×6) neighboring Fe should be detected in SHCa-1 and SapCa-2, respectively, which is below or at the detection limit. Low number of Fe–Fe pairs were detected ($N_{\mathrm{Fe1}} = 0.1$–0.2, Table 6) in both compounds suggesting a slight tendency of Fe pairs formation, in agreement with earlier findings (Finck et al. 2015). Note that preferential location of Fe–Fe pairs at platelet edges would also account for the low number of detected octahedral neighbors, at least in SapCa-2 which does not contain Li(I) and for which N_{O3} and N_{O4} are lower (Table 6) than expected for random distribution within the bulk structure.

In nontronites, the layer charge results predominantly from substitution within the tetrahedral sheet. In the FTIR spectrum of NG-1, the band at 840 cm^{-1} is of higher intensity than in the NAu-1 and NAu-2 spectra, and does not contain the $Fe^{3+}Al^{3+}$–OH-bending band at 860 cm^{-1} (Fig. 3). This result suggests that the band at 840 cm^{-1} possibly results from an overlap of the $Fe^{3+}{}_2$–OH and the $Al^{3+}Mg^{2+}$–OH-bending bands, which would mean that Al has a tendency to form pairs with Mg in NG-1 and seem to agree with earlier P-EXAFS studies (Manceau et al. 2000). NAu-1 and NAu-2 have similar Mg contents, but NAu-1 lacks the $Fe^{3+}Mg^{2+}$–OH-bending band at 787 cm^{-1} in contrast to NAu-2, meaning that Mg has a tendency to form pairs with Fe in NAu-2 but not in NAu-1. Analyses showed that these nontronites have comparable chemical composition, but FTIR data indicate differences in distribution of cations within the clay sheets. Polarized XAS data rule out the presence of $^{[4]}Fe^{3+}$ in NAu-1 and NAu-2 (up to the detection limit), but hint at the simultaneous presence of $^{[4]}Fe^{3+}$ and $^{[6]}Fe^{3+}$ in NG-1.

Both synthetic saponites only contain Mg in the octahedral sheet, and Fe (plus Al) substituting for Si in the tetrahedral sheet. An unambiguous signature is the characteristic $^{[4]}Fe^{3+}$–O vibration at 720 cm^{-1} in the FTIR spectra (Fig. 3) and the intensity of this band parallels the $^{[4]}$Fe content. However, this band could not be detected in the NG-1 spectrum, the only nontronite containing tetrahedral Fe, possibly because of the low $^{[4]}$Fe content. The spectra of synthetic saponites markedly differ from that of synthetic nontronites (Baron et al. 2016) because of differences in the octahedral framework, synthetic saponites are thus free from synthetic nontronite. In synthetic saponites, only tetrahedral Fe could be detected by XAS, and the low number of $^{[4]}$Fe–$^{[4]}$Fe pair indicates a fully random distribution within the tetrahedral sheet. The angular dependence of contributions from neighboring cationic shells excludes the presence of octahedral ferric iron in these samples. The synthesis of saponite containing tetrahedral Fe(III) thus operates under defined conditions in the laboratory.

Conclusion

Smectites of various chemical compositions and charge locations were selected to explore the variety of Fe crystallochemistry. Synthetic trioctahedral saponites contain only Fe(III) substituting for Si in the tetrahedral sheet, with a first coordinating O shell at 1.86 Å. In natural dioctahedral smectites, Fe is bound to six O atoms oriented in-plane at a distance of ~ 2.00 Å. The insertion in octahedral sites is corroborated by the detection of three in-plane Mg/Al/Fe atoms at ~ 3.05 Å and four out-of-plane Si/Al at ~ 3.25 Å. The low number of detected Fe backscatterers in montmorillonite suggests homogeneous distribution within the octahedral sheet. For one nontronite particularly rich in Fe, EXAFS data suggest a concomitant Fe insertion in the tetrahedral sheet, in agreement with earlier studies. In natural trioctahedral saponite and hectorite, only sixfold coordinated Fe(III) could be observed but low number of octahedral neighbors were detected. The substitution of Fe(III) for Mg(II) creates an excess charge that may be balanced either by vacancies in adjacent octahedral sites or by insertion of Li(I) substituting for Mg(II) in hectorite, in agreement with earlier studies (Finck et al. 2015). No extensive clustering could be detected in either mineral, indicating a close to random distribution of Fe.

Smectites with defined Fe crystallochemical environments can be prepared in the laboratory, and are necessary reference compounds in the analysis of natural samples. All natural smectites contain octahedral Fe(III); however, the structure seems also flexible enough to allow Fe(III) substitution for tetrahedral Si despite the difference in ionic radii. However, Fe(III) incorporation in tetrahedral sheets of natural smectites is rather limited, but may occur in amounts below the detection limit of EXAFS spectroscopy, especially in dioctahedral smectites (Kaufhold et al. 2017). Because most of structural Fe is located at octahedral sites, it can be reduced to Fe(II), and thereby alter the physicochemical properties of smectites, and consequently, the retention properties of bentonite used as engineered barriers in deep disposal sites. Similar investigations on structural characterization with special attention to structural Fe in smectites, yet performed under conditions more representative of disposal sites (e.g., anoxic, reducing, elevated temperature) would help improving the scientific basis for performance assessment of such repositories.

Acknowledgements We acknowledge the contribution of the late Dr. J.-L. Robert of IMPMC to this work. We thank E. Soballa (KIT-INE) for SEM-EDX analyses. We acknowledge the KIT Synchrotron Light Source and the Institute for Beam Physics and Technology (IBPT) for operation of the storage ring, the Karlsruhe Research Accelerator (KARA). We also thank the ESRF for provision of synchrotron radiation beam time and I. Kieffer for support at the BM30B (ESRF) beamline.

References

Ankudinov AL, Ravel B, Rehr JJ, Conradson SD (1998) Real-space multiple-scattering calculation and interpretation of X-ray-absorption near-edge structure. Phys Rev B 58(12):7565–7576

Bailey SW (1980) Structures of layer silicates. In: Brindley GW, Brown G (eds) Crystal structures of clay minerals and their X-Ray identification. Mineralogical society, London, pp 2–123

Baron F, Petit S, Tertre E, Decarreau A (2016) Infuence of aqueous Si and Fe speciation on tetrahedral Fe(III) substitutions in nontronites: a clay synthesis approach. Clays Clay Miner 64(3):230–244

Bishop ME, Dong HL, Kukkadapu RK, Liu CX, Edelmann RE (2011) Bioreduction of Fe-bearing clay minerals and their reactivity toward pertechnetate (Tc-99). Geochim Cosmochim Acta 75(18):5229–5246

Breu J, Seidl W, Stoll A (2003) Disorder in smectites in dependence of the interlayer cation. Z Anorg Allg Chem 629(3):503–515

Brindley GW (1980) Order-disorder in clay mineral structures. In: Brindley GW, Brown G (eds) Crystal structures of clay minerals and their X-ray identification. Mineralogical Society, London, pp 125–195

Cadars S, Guégan R, Garaga MN, Bourrat X, Le Forestier L, Fayon F, Huynh TV, Allier T, Nour Z, Massiot D (2012) New insights into the molecular structures, compositions, and cation distributions in synthetic and natural montmorillonite clays. Chem Mater 24(22):4376–4389

Dong HL, Jaisi DP, Kim J, Zhang GX (2009) Microbe-clay mineral interactions. Am Miner 94(11–12):1505–1519

Drits VA, Manceau A (2000) A model for the mechanism of Fe^{3+} to Fe^{2+} reduction in dioctahedral smectites. Clays Clay Miner 48(2):185–195

Ernstsen V, Gates WP, Stucki JW (1998) Microbial reduction of structural iron in clays—a renewable source of reduction capacity. J Environ Qual 27(4):761–766

Favre F, Tessier D, Abdelmoula M, Génin JM, Gates WP, Boivin P (2002) Iron reduction and changes in cation exchange capacity in intermittently waterlogged soil. Eur J Soil Sci 53(2):175–183

Fialips CI, Huo D, Yan LB, Wu J, Stucki JW (2002) Infrared study of reduced and reduced-reoxidized ferruginous smectite. Clays Clay Miner 50(4):455–469

Finck N, Schlegel ML, Bosbach D (2009) Sites of Lu(III) sorbed to and coprecipitated with hectorite. Environ Sci Technol 43(23):8807–8812

Finck N, Schlegel ML, Bauer A (2015) Structural iron in dioctahedral and trioctahedral smectites: a polarized XAS study. Phys Chem Miner 42(10):847–859

Gates WP (2005) Infrared spectroscopy and the chemistry of dioctahedral smectites. In: Kloprogge T (ed) Vibrational spectroscopy of layer silicates and hydroxides, CMS workshop lecture series, vol 13. The Clay Mineral Society, Chantilly, pp 125–168

Gates WP (2008) Cation mass-valence sum (CM-VS) approach to assigning OH-bending bands in dioctahedral smectites. Clays Clay Miner 56(1):10–22

Gates WP, Stucki JW, Kirkpatrick RJ (1996) Structural properties of reduced Upton montmorillonite. Phys Chem Miner 23(8):535–541

Gates WP, Slade PG, Manceau A, Lanson B (2002) Site occupancies by iron in nontronites. Clays Clay Miner 50(2):223–239

Gorski CA, Klupfel LE, Voegelin A, Sander M, Hofstetter TB (2013) Redox properties of structural Fe in clay minerals: 3. Relationships between smectite redox and structural properties. Environ Sci Technol 47(23):13477–13485

Hofstetter TB, Neumann A, Schwarzenbach RP (2006) Reduction of nitroaromatic compounds by Fe(II) species associated with iron-rich smectites. Environ Sci Technol 40(1):235–242

Jaisi DP, Dong H, Plymale AE, Fredrickson JK, Zachara JM, Heald S, Liu C (2009) Reduction and long-term immobilization of technetium by Fe(II) associated with clay mineral nontronite. Chem Geol 264(1):127–138

Joe-Wong C, Brown GE, Maher K (2017) Kinetics and products of chromium(VI) reduction by iron(II/III)-bearing clay minerals. Environ Sci Technol 51(17):9817–9825

Kaufhold S, Stucki JW, Finck N, Steininger R, Zimina A, Dohrmann R, Ufer K, Pentrák M, Pentráková L (2017) Tetrahedral charge and Fe content in dioctahedral smectites. Clay Miner 52(1):51–65

Keeling JL, Raven MD, Gates WP (2000) Geology and characterization of two hydrothermal nontronites from weathered metamorphic rocks at the Uley Graphite Mine, South Australia. Clays Clay Miner 48(5):537–548

Khaled EM, Stucki JW (1991) Iron oxidation state effects on cation fixation in smectites. Soil Sci Soc Am J 55(2):550–554

Komarneni S, Fyfe CA, Kennedy GJ, Strobl H (1986) Characterization of synthetic and naturally-occuring clays by Al-27 and Si-29 magic angle spinning NMR spectroscopy. J Am Ceram Soc 69(3):C45–C47

Labouriau A, Kim YW, Earl WL (1996) Nuclear-spin-lattice relaxation in natural clays via paramagnetic centers. Phys Rev B 54(14):9952–9959

Lear PR, Stucki JW (1989) Effects of iron oxidation state on the specific surface area of nontronite. Clays Clay Miner 37(6):547–552

Lippmaa E, Mägi M, Samson A, Engelhardt G, Grimmer A-R (1980) Structural studies of silicates by solid-state high-resolution ^{29}Si NMR. J Am Chem Soc 102(15):4889–4893

Madejova J, Komadel P (2001) Baseline studies of the clay minerals society source clays: infrared methods. Clays Clay Miner 49(5):410–432

Manceau A (1990) Distribution of cations among the octahedra of phyllosilicates—insight from EXAFS. Can Mineral 28:321–328

Manceau A, Schlegel ML (2001) Texture effect on polarized EXAFS amplitude. Phys Chem Miner 28(1):52–56

Manceau A, Chateigner D, Gates WP (1998) Polarized EXAFS, distance-valence least-squares modeling (DVLS), and quantitative texture analysis approaches to the structural refinement of Garfield nontronite. Phys Chem Miner 25(5):347–365

Manceau A, Lanson B, Drits VA, Chateigner A, Gates WP, Wu. J, Huo D, Stucki. JW (2000) Oxidation-reduction mechanism of iron in dioctahedral smectites: I. Crystal chemistry of oxidized reference nontronites. Am Miner 85(1):133–152

Mering J, Oberlin A (1967) Electron-optical study of smectites. Clays Clay Miner 15(1):3–25

Méring J, Glaeser R (1953) Sur le rôle de la valence des cations échangeables dans la montmorillonite. Bull Soc Fr Minéral Cristallogr 77:519–530

Mermut AR, Cano AF (2001) Baseline study of the clay minerals society source clays: chemical analyses of major elements. Clays Clay Miner 49(5):381–386

Meunier A (2005) Clays. Springer-Verlag, Berlin Heidelberg, p 472

Michot LJ, Bihannic I, Pelletier M, Rinnert E, Robert JL (2005) Hydration and swelling of synthetic Na-saponites: Influence of layer charge. Am Miner 90(1):166–172

Moore DM, Reynolds RC Jr (1997) X-ray diffraction and the identification and analysis of clay minerals. Oxford University Press, Oxford, p 400

Morris HD, Bank S, Ellis PD (1990) Al-27 NMR spectroscopy of iron-bearing montmorillonite clays. J Phys Chem 94(7):3121–3129

Munoz M, Vidal O, Marcaillou C, Pascarelli S, Mathon O, Farges F (2013) Iron oxidation state in phyllosilicate single crystals using Fe-K pre-edge and XANES spectroscopy: effects of the linear polarization of the synchrotron X-ray beam. Am Miner 98(7):1187–1197

Neumann A, Petit S, Hofstetter TB (2011) Evaluation of redox-active iron sites in smectites using middle and near infrared spectroscopy. Geochim Cosmochim Acta 75(9):2336–2355

Prietzel J, Thieme J, Eusterhues K, Eichert D (2007) Iron speciation in soils and soil aggregates by synchrotron-based X-ray microspectroscopy (XANES, mu-XANES). Eur J Soil Sci 58(5):1027–1041

Proux O, Nassif V, Prat A, Ulrich O, Lahera E, Biquard X, Menthonnex J-J, Hazemann J-L (2006) Feedback system of a liquid-nitrogen-cooled double-crystal monochromator: design and performances. J Synchrotron Radiat 13:59–68

Ravel B, Newville M (2005) ATHENA, ARTEMIS, HEPHAESTUS: data analysis for X-ray absorption spectroscopy using IFEFFIT. J Synchrotron Radiat 12:537–541

Rothe J, Butirin S, Dardenne K, Denecke MA, Kienzler B, Löble M, Metz V, Seibert A, Steppert M, Vitova T, Walther C, Geckeis H (2012) The INE-beamline for actinide science at ANKA. Rev Sci Instrum 83(4):13

Sanz J, Serratosa JM (1984a) Distinction of tetrahedrally and octahedrally coordinated Al in phyllosilicates by NMR spectroscopy. Clay Miner 19(1):113–115

Sanz J, Serratosa JM (1984b) Si-29 and Al-27 high-resolution MAS NMR spectra of phyllosilicates. J Am Chem Soc 106(17):4790–4793

Schlegel ML, Manceau A (2013) Binding mechanism of Cu(II) at the clay-water interface by powder and polarized EXAFS spectroscopy. Geochim Cosmochim Acta 113:113–124

Schlegel ML, Manceau A, Chateigner D, Charlet L (1999) Sorption of metal ions on clay minerals I. Polarized EXAFS evidence for the adsorption of Co on the edges of hectorite particles. J Colloid Interface Sci 215(1):140–158

Semenova TF, Rozhdestvenskaya IV, Frankkamenetsky VA (1977) Refinement of the crystal structure of tetraferriphlogopite. Kristallografiya 22(6):1196–1201

Shannon RD (1976) Revised effective ionic radii and systematic studies of interatomic distances in halides and chalcogenides. Acta Crystallogr Sect A 32(SEP1):751–767

Stucki JW, Roth CB (1977) Oxidation-reduction mechanism for structural iron in nontronite. Soil Sci Soc Am J 41(4):808–814

Stucki JW, Golden DC, Roth CB (1984a) Effects of reduction and reoxidation of structural iron on the surface area and dissolution of dioctahedral smectites. Clays Clay Miner 32(5):350–356

Stucki JW, Low PF, Roth CB, Golden DC (1984b) Effects of oxidation state of octahedral iron on clay swelling. Clays Clay Miner 32(5):357–362

Thomas J, Glass HD, White WA, Trandel RM (1977) Fluoride content of clay minerals and argillaceous earth materials. Clays Clay Miner 25(4):278–284

Tsipursky SI, Drits VA (1984) The distribution of octahedral cations in the 2:1 layers of dioctahedral smectites studied by oblique-texture elecron diffraction. Clay Miner 19(2):177–193

Vantelon D, Montarges-Pelletier E, Michot LJ, Briois V, Pelletier M, Thomas F (2003) Iron distribution in the octahedral sheet of dioctahedral smectites. An Fe K-edge X-ray absorption spectroscopy study. Phys Chem Miner 30(1):44–53

Waychunas GA, Apted MJ, Brown GE (1983) X-ray K-edge absorption spectra of Fe minerals and model compounds: Near-edge structure. Phys Chem Miner 10(1):1–9

Westre TE, Kennepohl P, DeWitt JG, Hedman B, Hodgson KO, Solomon EI (1997) A multiplet analysis of Fe K-edge 1 s→3d pre-edge features of iron complexes. J Am Chem Soc 119(27):6297–6314

Wilke M, Farges F, Petit PE, Brown GE, Martin F (2001) Oxidation state and coordination of Fe in minerals: an Fe K-XANES spectroscopic study. Am Miner 86(5–6):714–730

Woessner DE (1989) Characterization of clay minerals by Al-27 nuclear magnetic resonance spectroscopy. Am Miner 74(1–2):203–215

Empfohlene Zitierung:

Finck, N.; Schlegel, M. L.; Dardenne, K.; Adam, C.; Kraft, S.; Bauer, A.; Robert, J.-L.
Structural iron in smectites with different charge locations
2019. Physics and chemistry of minerals, 46. doi: 10.5445/IR/1000094341

Zitierung der Originalveröffentlichung:

Finck, N.; Schlegel, M. L.; Dardenne, K.; Adam, C.; Kraft, S.; Bauer, A.; Robert, J.-L.
Structural iron in smectites with different charge locations
2019. Physics and chemistry of minerals, 46, 639–661. doi:10.1007/s00269-019-01028-y